



**AN ANALYSIS OF THE POTENTIAL FOR USING OVER-THE-HORIZON  
RADAR SYSTEMS FOR SPACE SURVEILLANCE**

**THESIS**

Matthew J. Colbert, Flight Lieutenant, Royal Australian Air Force

AFIT/GSS/ENG/04-01

**DEPARTMENT OF THE AIR FORCE  
AIR UNIVERSITY**

**AIR FORCE INSTITUTE OF TECHNOLOGY**

---

---

**Wright-Patterson Air Force Base, Ohio**

**APPROVED FOR PUBLIC RELEASE; DISTRIBUTION UNLIMITED**

The views expressed in this thesis are those of the author and do not reflect the official policy or position of the United States Air Force, Department of Defense, the U.S. Government, the Royal Australian Air Force, Department of Defence, or the Australian Government.

AFIT/GSS/ENG/04-01

**AN ANALYSIS OF THE POTENTIAL FOR USING OVER-THE-HORIZON  
RADAR SYSTEMS FOR SPACE SURVEILLANCE**

**THESIS**

Presented to the Faculty

Department of Electrical and Computer Engineering

Graduate School of Engineering and Management

Air Force Institute of Technology

Air University

Air Education and Training Command

In Partial Fulfillment of the Requirements for the

Degree of Master of Science in Space Systems

Matthew Colbert, BE

Flight Lieutenant, Royal Australian Air Force

March 2004

APPROVED FOR PUBLIC RELEASE; DISTRIBUTION UNLIMITED

**AN ANALYSIS OF THE POTENTIAL FOR USING OVER-THE-HORIZON  
RADAR SYSTEMS FOR SPACE SURVEILLANCE**

Matthew Colbert, BE

Flight Lieutenant, Royal Australian Air Force

Approved:

//SIGNED//  
Maj. Todd B. Hale, PhD, USAF (Chairman)

12 Mar 03  
Date

//SIGNED//  
Dr. Michael Temple (Member)

12 Mar 03  
Date

//SIGNED//  
Dr. Steven T. Tragesser (Member)

12 Mar 03  
Date

//SIGNED//  
Maj. Clark M. Groves, USAF (Member)

12 Mar 03  
Date

## **Acknowledgments**

I would like to express my sincere appreciation to my thesis advisor, Major Todd Hale, for his guidance, commitment and encouragement throughout this thesis effort. His insight and experience was certainly appreciated, as were his patient endeavors to teach me about radar signal processing, outside of his regular course program. I would also like to thank my other thesis committee members, Dr. Michael Temple, Major Clark Groves, and Dr. Steven Tragesser, for their valuable input.

My fellow students at AFIT have made me feel very welcome, so that I barely noticed being 15000 km (9500 miles) away from home. My exposure to American culture has broadened my horizons immeasurably, and I will keep the friends I have made here for life.

My experiences at AFIT were greatly enhanced by the efforts of the International Affairs director, Mrs. Annette Robb as well as Janice, Lynn and Valerie. They made my course through the turbid waters of an unfamiliar administrative system much simpler.

Finally, to my wife, thank you for your support and sacrifices during the entire course. I look forward to making your acquaintance, again.

Matthew Colbert

## Table of Contents

	Page
Acknowledgments.....	iv
Table of Contents.....	v
List of Figures .....	ix
List of Tables .....	xi
Abstract.....	xii
1. Introduction .....	1
1.1 Background .....	1
1.2 Problem Statement .....	1
1.3 Research Objectives/Focus .....	2
1.4 Methodology .....	2
1.5 Assumptions and Limitations.....	2
1.6 Preview.....	3
2. Background and Literature Review.....	5
2.1 Chapter Overview .....	5
2.2 Introduction to Over-The-Horizon Radar .....	5
2.2.1 <i>Current Roles of OTHR</i> .....	6
2.3 OTHR Research .....	7
2.4 The Ionosphere .....	8
2.4.1 <i>Structure</i> .....	9
2.4.2 <i>Radio Propagation</i> .....	9
2.4.3 <i>Ionospheric Motion</i> .....	10
2.5 Antenna Arrays .....	10

2.6	Radar Models .....	11
2.7	Clutter Modeling .....	11
2.8	Target Characteristics.....	12
2.8.1	<i>Trajectories</i> .....	12
2.8.2	<i>Radar Cross-Section</i> .....	13
3.	Ionospheric Model.....	15
3.1	Chapter Overview .....	15
3.2	General Considerations .....	15
3.3	Ionospheric Structure .....	15
3.3.1	<i>Radio Signal Propagation</i> .....	16
3.3.2	<i>Cutoff Angles</i> .....	21
3.3.3	<i>Path Lengths to Ground</i> .....	21
3.4	Summary .....	22
4.	Radar Model .....	25
4.1	Chapter Overview .....	25
4.2	General Considerations .....	25
4.3	Antenna Model .....	26
4.3.1	<i>Dipole Pattern</i> .....	26
4.3.2	<i>Monopole Pattern</i> .....	27
4.3.3	<i>Array Factor</i> .....	30
4.3.4	<i>Overall Antenna Pattern</i> .....	32
4.4	Thermal Noise .....	38
4.5	Clutter Model .....	39

4.5.1	<i>Geometry</i> .....	39
4.5.2	<i>Range to Clutter Rings</i> .....	42
4.5.3	<i>Clutter Return Power</i> .....	46
4.5.4	<i>Clutter Covariance</i> .....	48
4.6	Atmospheric Noise and Interference.....	50
4.7	Total Interference .....	50
4.7.1	<i>Statistical Realization</i> .....	51
4.8	Clutter Structure .....	53
4.9	Summary .....	56
5.	Analysis of Results.....	58
5.1	Chapter Overview .....	58
5.2	General Considerations .....	58
5.3	Noise Limited Case .....	58
5.4	Introduction of Clutter.....	60
5.5	Target Detection in Clutter.....	61
5.6	Limits on Coherent Pulse Integration.....	65
5.7	Limits on Doppler Space.....	65
5.8	Interpulse Modulation .....	66
5.9	Internal Clutter Motion.....	68
5.10	Summary .....	69
6.	Conclusions and Recommendations.....	71
6.1	Overview .....	71
6.2	Conclusions of Research .....	72

6.3	Significance of Research.....	73
6.4	Recommendations for Action.....	73
6.5	Recommendations for Future Research .....	74
6.6	Summary .....	74
	Bibliography .....	75
	Vita .....	78

## List of Figures

	Page
Figure 1. Conceptual OTHR diagram.....	6
Figure 2. Electron density profile vs. altitude for daytime ionosphere under moderate solar activity.....	17
Figure 3. Angles of incidence and refraction in spherical layers.....	19
Figure 4. Path profiles for $10^\circ$ , $25^\circ$ , $38^\circ$ and $45^\circ$ elevation angles at $f = 30$ MHz.....	20
Figure 5. Path profiles for $10^\circ$ , $25^\circ$ , $38^\circ$ and $45^\circ$ elevation angles at $f = 15$ MHz.....	20
Figure 6. Path profiles for elevation angles from $1-90^\circ$ .....	22
Figure 7. Path plots of E, F1 and F2 layer propagation modes.....	23
Figure 8. Combination of direct and reflected rays. ....	28
Figure 9. Angles of incident and reflected rays.....	29
Figure 10. Polar view of element gain pattern, $f = 30$ MHz.....	30
Figure 11. Monopole element pattern for $f = 30$ MHz.....	31
Figure 12. Detail of monopole element pattern, $f = 30$ MHz.....	31
Figure 13. Array factor, $f = 30$ MHz.....	33
Figure 14. Main lobe of array factor, $f = 30$ MHz. ....	33
Figure 15. Resultant antenna pattern, $f = 30$ MHz.....	34
Figure 16. Main lobe and principle sidelobes of antenna pattern, $f = 30$ MHz. ....	35
Figure 17. Top view of main lobe showing zeros between lobes, $f = 30$ MHz .....	35
Figure 18. Cross sectional view of main lobe for $12^\circ$ elevation angle, at main lobe peak, for $f = 30$ MHz.....	36
Figure 19. Cross sectional view of antenna pattern for $90^\circ$ azimuth angle, at main lobe peak, for $f = 30$ MHz. ....	37
Figure 20. Radiated power distribution with the antenna pattern superimposed.....	37
Figure 21. Clutter ring geometry, showing ranges and elevation/grazing ( $\psi$ ) and azimuth ( $\phi$ ) angles.....	40
Figure 22. Example of two different clutter patches at the same path length.....	41
Figure 23. Range (path length) to clutter ring vs. elevation angle, with angles calculated at $0.1^\circ$ intervals.....	42
Figure 24. Range (path length) to clutter ring vs. elevation angle of interpolated paths, at increments of $10^{-2^\circ}$ .....	44
Figure 25. Folded clutter range (path length) vs. elevation angle for $f_p = 200$ Hz and $\Delta\theta = 10^{-2^\circ}$ .....	45
Figure 26. Number of clutter rings in each range bin, for $f_p = 200$ Hz and $\Delta\theta = 10^{-2^\circ}$ .....	45
Figure 27. Number of clutter rings in each range bin, for $f_p = 200$ Hz and $\Delta\theta = 10^{-3^\circ}$ .....	46
Figure 28. Number of clutter rings in each range bin, with duplicates removed, for $f_p = 200$ Hz and $\Delta\theta = 10^{-3^\circ}$ .....	47
Figure 29. SINR per element, per pulse, for $P_{fa}=10^{-3}$ .....	53
Figure 30. Minimum Variance Power Spectral Density of clutter, for $f_p = 200$ Hz and $M = 10$ .....	55

Figure 31. Fourier Power Spectral Density of clutter, for $f_p = 200$ Hz and $M = 10$ .....	56
Figure 32. Minimum variance Power Spectral Density of clutter, for $f_p = 200$ Hz and $M = 30$ .....	57
Figure 33. Fourier Power Spectral Density of clutter, for $f_p = 200$ Hz and $M = 30$ .....	57
Figure 34. Minimum Target RCS vs. Range, noise only, for $P_{fa} = 0.01$ and $P_d = 0.95$ . ..	59
Figure 35. Clutter power seen at each range bin, for $f_p = 200$ Hz.....	62
Figure 36. Minimum target radar cross-section vs. range for $f_p = 200$ Hz, no pulse integration, over the radar's unambiguous range.....	62
Figure 37. Minimum radar cross-section for $M = 10$ , with $f_p = 200$ Hz and $f_d = 850$ Hz, for a representative set of target ranges.....	63
Figure 38. Minimum radar cross-section vs. Doppler frequency for $f_p = 200$ Hz and $M = 10$ pulses, target range = 320 km.....	64
Figure 39. Minimum radar cross-section vs. Doppler frequency for $f_p = 200$ Hz and $M = 20$ pulses, target range = 320 km.....	64
Figure 40. Minimum target RCS for $f_p = 1200$ , $M = 10$ , 16 interpulse codes, with target range = 320 km.....	67
Figure 41. Fourier PSD for $f_p = 1200$ , $M = 10$ , 16 interpulse codes, with range = 320 km. The Doppler side lobes are now greatly reduced.....	68
Figure 42. Minimum RCS for $f_p = 1200$ , $M = 10$ , 16 pulse coding, with range = 320 km, with ICM included.....	69

## **List of Tables**

	Page
Table 1. Antenna Parameters .....	11

## **Abstract**

The Australian Defence Force is investigating the development of a space surveillance system. While several dedicated facilities for space surveillance are in operation around the world, Australia's Over-The-Horizon Radar (OTHR) network has some potential for this role.

The OTHR operates in the HF band and is constrained by the propagation effects of the ionosphere. A spherically stratified ionospheric model and a model for a nominal OTHR antenna are developed that allow calculation of path propagation, power distribution, and clutter returns. A software-based radar receiver processing system is modeled to determine detection probabilities and the minimum detectable radar cross-section of targets in typical low earth orbit (LEO) trajectories. The high clutter power levels, coupled with long target ranges and high velocities, mean that range-Doppler tradeoffs have a great impact on the resulting detection capabilities.

While the system as modeled has the potential to provide some coverage for LEO targets, operational constraints mean the necessary conditions for detection of space targets would rarely be met while the system is involved in traditional OTHR tasking. Further, the long wavelengths and large antenna beams mean the accuracy of any positioning information is low.

# **AN ANALYSIS OF THE POTENTIAL FOR USING OVER-THE-HORIZON RADAR SYSTEMS FOR SPACE SURVEILLANCE**

## **I. Introduction**

### **1.1 Background**

The Australian Defence Force is interested in developing a capability for space surveillance from the ground. While dedicated space surveillance facilities exist in other defense forces and similar systems would be suitable for Australia's needs, the Royal Australian Air Force (RAAF) currently operates a network of over-the-horizon radars (OTHRs) that has potential for space surveillance.

While OTHR<sup>s</sup> are not ideal for the space surveillance role and cannot provide the same level of performance as dedicated facilities, the use of existing systems would provide substantial cost savings and is worthy of investigation.

There is also potential for international cooperation in space surveillance. The USAF Science Advisory Board report on the US Space Surveillance Network [16:8-9] recognizes deficiencies in the network's coverage near Asia and in the southern hemisphere. A space surveillance system in Australia could partially fill this gap.

### **1.2 Problem Statement**

This thesis examines the potential for using over-the-horizon radar in a space surveillance role and describes the performance of an OTHR in certain scenarios.

### **1.3 Research Objectives/Focus**

The research described in this thesis aims to determine whether an OTHR system, despite its inherent limitations, can provide enough capability for space surveillance to warrant further research. This research focuses on using computer simulations to estimate target sizes and trajectories that could be detected by an OTHR.

Several important questions are addressed in determining the feasibility of using OTHR for the space surveillance role, including:

What coverage area can be obtained from such radars?

Within the coverage area, what types of targets can be detected?

What are the limitations on target trajectories?

How does ionospheric variation affect OTHR performance in this role?

### **1.4 Methodology**

Quantitative analysis of the problem requires a model with four main components: the antenna arrays, the ionosphere and path propagation, the radar and its clutter environment, and the target. The antenna arrays, ionosphere and radar clutter are modeled in Matlab<sup>®</sup>, from which conclusions about target characteristics can be made.

### **1.5 Assumptions and Limitations**

Several simplifications are necessary to limit the scope of the problem. The most significant is the simplified ionospheric model. The real ionosphere has a complicated structure with high variability in space and time. This structure alone is the subject of much continuing research. Operational OTMRs require extensive ionospheric sounding

systems to maintain sufficiently accurate models. The model used in this paper treats the ionosphere as spherically stratified—uniform layers of constant density at a given altitude.

Another simplification is that most OTHR systems are bistatic, while this thesis uses a monostatic model. This change allows simplified path propagation and clutter geometry without having a major impact on the results. Path propagation effects are the major difference between the bistatic and monostatic cases; however, the simplifications made in the ionospheric model mean that target placement can account for this difference.

A third major assumption is that the operating frequency spectrum of the OTHR is sufficient to allow operation in a channel that is relatively free of other transmitters. This assumption means system performance is limited by clutter whereas interfering transmitters can sometimes be a limiting factor in real operations.

Lastly, most OTHR systems operate using frequency modulated, continuous wave (FM-CW) signals, to allow for greater transmission efficiency at the cost of requiring separate transmitter and receiver sites. This thesis is limited to a pulsed waveform, which allows a simplified detection model. Although the operating parameters of pulsed and FM-CW radars differ, parallels can be drawn between the two methods to allow comparison of results.

## 1.6 Preview

This research shows that an OTHR, while showing some potential for use in a space surveillance role, has significant limitations. The primary limitation is that an

OTHR can not simultaneously perform its ordinary surveillance tasks and space surveillance tasks. Further, the information derived about space targets is limited.

## **II. Background and Literature Review**

### **2.1 Chapter Overview**

Existing research into over-the-horizon radar (OTHR) draws from several fields including radar theory, High Frequency (HF) communications, ionospheric physics, remote sensing, and oceanography. This chapter describes the relevant research and its use in this thesis.

### **2.2 Introduction to Over-The-Horizon Radar**

Military forces have used Radio Detection and Ranging (RADAR) for surveillance since WWII. Traditional radars are limited in coverage to the radio horizon, just beyond the visible horizon. Surveillance of large areas then requires multiple radars with operational and management overheads to combine the sensor data.

Electronics technology limited early radar operations to the HF band. This band has many disadvantages for radar including large antennas, high ambient interference levels, and a narrow and often congested spectrum [20:1.15]. For these reasons, the HF band is no longer used for radar with one important exception: over-the-horizon radar (OTHR).

OTHR was explored in the late 1940s and developed in the ensuing decades until several systems were fielded from the 1960's onwards [5]. Like short-wave radio, OTHR takes advantage of ionospheric refraction properties, allowing the radar to ‘see’ far beyond the optical horizon. This advantage provides a workable range of approximately 1500-3000 km for aircraft-sized targets and gives a means of observing large areas (such

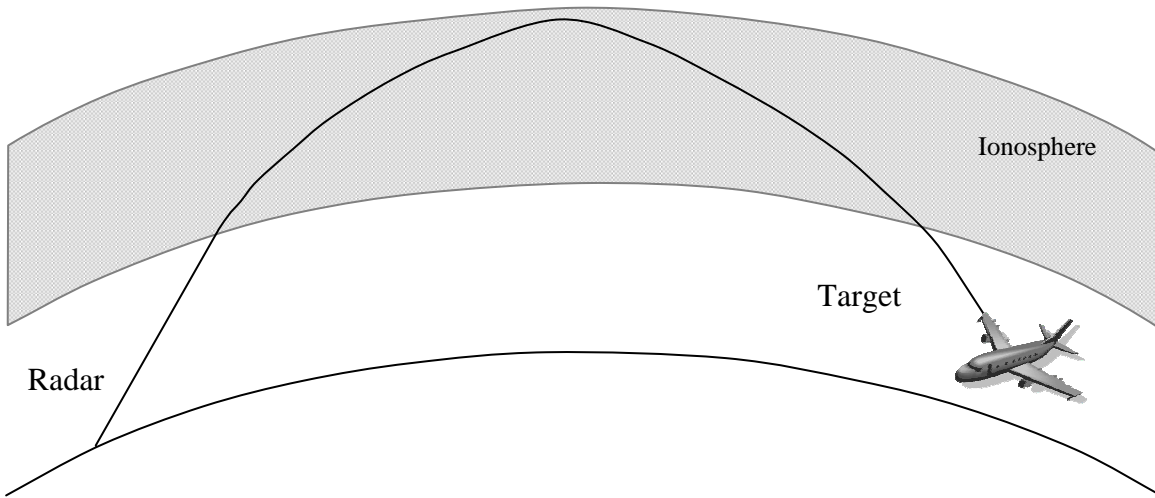


Figure 1. Conceptual OTHR diagram, showing the refracted signal path to a target beyond visual range.

as oceans) that would not be practical with conventional microwave radar. The basic concept of OTHR operation is illustrated in Figure 1.

### ***2.2.1 Current Roles of OTHR***

One main driver for early research into OTHR was detection of ICBM launches, although satellite-based systems have largely supplanted OTHRs in this role. Other applications include surveillance for aircraft or ships, as well as ionospheric sounding, ocean wave detection and remote sensing [3].

Australia's Department of Defence uses the Jindalee Operational Radar Network (JORN) to monitor its northern maritime approaches. Similarly, the United States Drug Enforcement Agency uses the US Navy's Relocatable OTHRs to monitor the Florida Keys and surrounding waters. The National Oceanic and Atmospheric Administration's (NOAA) Environmental Technology Laboratory (ETL) also has occasional access to the USN Relocatable OTHRs for oceanographic monitoring. In Australia's case, the population is concentrated along the eastern, southern and southwestern coastlines, while

the closest approaches from neighboring countries are from the north and north-west.

OTHR is ideal as it allows monitoring of the entire northern region with only two facilities.

Space surveillance of is one potential role that has seen little exploration. VHF, UHF and SHF systems are used in various locations for space surveillance, however HF, OTHR systems have not been examined for this role.

### 2.3 OTHR Research

Numerous papers and at least one text are devoted to various aspects of OTHR. A primary resource for much of the background of this thesis was Kolosov [13]. Kolosov describes the OTHR scenario from the very beginning, describing most aspects of the problem including transmitter and receiver equipment design, ionospheric transmission, target modeling, and passive and active interference. However, the book pre-dates many modern signal processing techniques, and so needs supplementation from modern radar research. Also, the book gives a mix of experimental, empirical and theoretical values for various parameters.

The USAF has published several papers describing its AN/FPS-118 Over-The-Horizon-Backscatter (OTH-B) systems, including the *OTH Handbook* [8] and Sales [19]. The ETL gives the relevant operating parameters for the OTH-B [17].

The prime contractor for the construction of the AN/FPS-118 OTH-B radars was Lockheed-Martin, the same company that completed the final stages of Australia's JORN. Photos of the two systems in [2] and [17] show striking similarities. Because

Australia's system is operational, detailed system parameters are classified, so this thesis uses the published parameters for the OTH-B.

To improve operational performance of OTHR systems, target track association has generated much research. There are many methods of performing this task, but all are based on statistical association processes. This thesis is limited to the problem of detection, and does not consider track association further.

In general, OTHR systems do not determine the height of a target. There are several proposed methods to estimate target height, mostly based on multipath association [18] but these methods rely on the target being near the ground and do not apply to space targets.

Other research includes methods to correlate returns from multiple OTHRs, such as [23], [24] and [27], improving the detection of targets moving tangentially to one of the radars. This approach has potential for use in orbit determination, but is not considered in this thesis.

## 2.4 The Ionosphere

The strong dependence of the radio signal path on the ionosphere means that a detailed, accurate, and timely ionospheric model is required for accurate prediction of paths and, consequently, target positioning.

A lot of research, such as [2], [4], [15] and [26], has gone into ionospheric modeling and the field is still evolving. High frequency (HF) communications systems are the drivers for much of this research; however, the same effects apply to OTHR.

While a complex model is required to operate an OTHR system, a simple, spherically-stratified ionospheric model provides enough fidelity to give representative performance.

#### ***2.4.1 Structure***

The ionosphere has an intricate structure, with electron density at a given time (and so refractive index) varying considerably laterally and with altitude. The variations in solar radiation, numerous chemical reactions, neutral atmosphere wind currents, and magnetic field interactions mean that the ionosphere has large, complex fluctuations over time. Some are periodic and predictable, while others are essentially random and cannot be modeled analytically.

The ionosphere has identifiable layers, known as D, E, F1 and F2. These designations are historical, and bear no relation to the properties of each layer. The ionization in the D layer consists mainly of heavy ions, and has an absorptive effect on radio signals, while the ionization in the E, F1 and F2 layers is mainly free electrons, which primarily have refractive effects.

#### ***2.4.2 Radio Propagation***

Tascione [22:113-117] and Collin [6:388-401] describe the effect of the ionosphere on radio signals. Tascione goes into detail about polarization effects and Faraday rotation of the signal, while Collin explores magnetic field interactions. However, these effects can be neglected without losing the representative system performance.

### **2.4.3 *Ionospheric Motion***

The irregularities in the ionosphere are subject to convective currents on both large and small scales. The resultant motion causes Doppler broadening of radio signals and spreading of clutter returns. The magnitude of the effect depends on operating frequency, path length and trajectory, and on the state of the ionosphere itself. In OTHR situations, the broadening bandwidth is typically around  $\pm 1$  Hz [19:22].

## **2.5 Antenna Arrays**

The antenna arrays used in OTHR are large but can be simply modeled using techniques described in [1], [6] and [14]. Most working parameters for the antennas are given by the ETL [17], but several lower level parameters for the electrical properties of the ground plane have been assumed, based on typical ranges. The resultant antenna pattern is most sensitive to the size and distance parameters with changes in ground plane electrical characteristics having a relatively small effect. The appropriate parameters are shown in Table 1.

These parameters apply to the receive array. The transmit array is more complex to handle the high power levels but has the same gain and beamwidth as the receive antenna. For the purpose of modeling, the transmit and receive antennas are treated as identical.

Table 1. Antenna Parameters

Parameter Name	Value
Element Separation	5.4 m
Element Height	10 m
Number of elements in array group	82
Transmitted power	12 MW
Height of bottom of element	0.1 m
Ground permeability	$\mu_0$
Ground conductivity	$10^4$ S/m
Ground permittivity	$10^2$ F/m

## 2.6 Radar Models

Much of the current research into radars and radar modeling involves Space-Time Adaptive Processing (STAP). The principles of STAP are described in Klemm [12], and are used in Hale [10]. Although the model used in this thesis is not adaptive, it uses the same framework.

## 2.7 Clutter Modeling

The problems of clutter modeling and clutter rejection in OTHR are the subject of many papers, but given an assumption about its distribution, the clutter can be modeled using variations of standard techniques. The statistical distribution of OTHR clutter has variously been modeled as Gaussian/Rayleigh, Gamma, Weibull and  $K$ -distribution, and at different times is seen to approach each of these distributions [28]. This paper takes the clutter distribution as Gaussian.

## 2.8 Target Characteristics

While most OTHR research is concerned with aircraft or ship targets, the same concepts apply to space-based targets.

### 2.8.1 Trajectories

The lower altitude limit for a space-based target is approximately 200 km, placing a lower limit on the range to the target. There is no theoretical upper limit on target altitude; however, this analysis is limited to low-earth-orbit (LEO) targets below 2000 km altitude.

Within this range of altitudes, circular orbits have velocities ranging from approximately 6.9 to 7.8 km/s. The target's orbit can have any orientation in relation to the radar; however, if the target trajectory passes directly along boresight of the radar antenna, this range of velocities gives the maximum Doppler frequency change. Elliptical and ballistic orbits can have velocities outside this range, but this velocity range is sufficient to analyze the system performance.

For a target passing directly overhead, the Doppler frequency  $f_d$  is given by

$$f_d = \frac{2v_t \cos \theta}{\lambda_0} \quad (1)$$

where  $v_t$  is the velocity of the target located at elevation  $\theta$ , and  $\lambda_0$  is the signal wavelength. A radar has a certain Doppler frequency range that it can correctly determine, known as the Doppler space. The high target velocities mean the requirement for Doppler space is a major driver on the radar performance requirements.

## 2.8.2 Radar Cross-Section

Due to the long wavelengths associated with OTHR operation, the radar cross-section (RCS) for many targets is significantly different to that seen by UHF or SHF radar. This thesis will not model specific targets, but will use typical values of RCS for comparison.

### 2.8.2.1 Rockets and Inter-Continental Ballistic Missiles

Both the body and the exhaust trail contribute to the RCS of a rocket. The radio waves scatter from the metal body of the rocket and also off the partially ionized exhaust stream. Because the structure of the exhaust stream changes continuously during flight, the scattered electromagnetic field components are non-coherent [13:93]. As a result, the radar return from the exhaust flame is independent of the return from the rocket body, and the RCS may be calculated as in (2), where  $\sigma_b$  and  $\sigma_{exh}$  refer to the rocket body and exhaust plume, respectively.

$$\sigma = \sigma_b + \sigma_{exh} \quad (2)$$

A rocket or ICBM body is essentially a cylinder and its RCS  $\sigma_b$  may be estimated by

$$\sigma_b = \frac{2\pi RL^2}{\lambda} \sin(\psi) \left[ \frac{\sin(2\pi L \lambda^{-1} \cos \psi)}{2\pi L \lambda^{-1} \cos \psi} \right] \quad (3)$$

where  $R$  is the radius of the missile body,  $L$  is its length,  $\lambda$  is the wavelength and  $\psi$  is the angle between the direction of the incident wave and the long axis of the missile [13:93].

With a missile body typically being ~10 to 20 m long and ~1 m wide, the RCS is typically from 5.0 to 50 m<sup>2</sup>, depending on wavelength and aspect.

The exhaust stream of a rocket starts small and lightly ionized, with an insignificant RCS. As the altitude increases, the exhaust stream RCS grows until, at approximately 60 km altitude (after first stage separation), it dwarfs the body RCS. In this case, the exhaust may have an RCS greater than 10000 m<sup>2</sup>. As the rocket continues upwards, the exhaust RCS decreases as the atmosphere becomes thinner and the ambient ionization levels are higher [13:96-98].

### **2.8.2.2 Satellites and Spacecraft**

Although there are a vast number of different satellite designs and configurations, practical satellites have a maximum size comparable to the wavelengths at the top of the HF band. The largest dimension of such satellites is normally that of the solar panels, stabilizing protrusions, or possibly antennas. Other satellite dimensions are small so the RCS is similar to that of a dipole reflector [11:24.11] or a cylinder.

Many satellites are smaller than the shortest HF wavelength, so the satellite shape becomes unimportant. These satellites have a response in the Rayleigh region and an RCS in the order of 0.1-1 m<sup>2</sup> [21:50-51].

### **III. Ionospheric Model**

#### **3.1 Chapter Overview**

The ionosphere refracts radio signals, with refraction varying depending on the signal frequency and on the state of the ionosphere. The refraction is important for an OTHR because it controls radar signal propagation. This chapter describes the effects of the ionosphere on high frequency signal propagation, its impact on OTHR operations, and how those effects are modeled in this research, as well as the simplifications necessary to allow analysis of the effects.

#### **3.2 General Considerations**

Completely describing the ionosphere and its effects on signal propagation requires an extremely complex model, which would overwhelm the other aspects of the OTHR scenario. Hence, this model takes a simple, spherically-stratified ionosphere with constituents that are typical under normal atmospheric conditions. The atmosphere also causes signal attenuation, but this effect is small and not included in the model.

These simplifications mean this model does not *accurately* describe any specific real-world situation; however, the model does allow realistic analysis of potential performance, with the ability to hold the ionosphere as a constant to evaluate the effect of other radar parameters.

#### **3.3 Ionospheric Structure**

The ionosphere is a region of the earth's atmosphere in which a significant proportion of the molecules are ionized. While there is no hard boundary to the region, it

is generally considered to lie from 90 to approximately 1000 km altitude, with the peak ionization lying near 300 km.

The ionosphere is quantified by the density of free electrons, with the density at a given time varying considerably laterally and with altitude. This electron density is the basis of propagation calculations in the atmosphere. Although the densities have large variations, there are typical values that are representative of the structure of the ionosphere, and these provide a basis for this ionospheric model.

The plot in Figure 2 shows the variation of the atmospheric electron density with altitude, using values typical for local daytime during a period of moderate solar activity (the middle of the 11-year sunspot cycle) [22:114-115]. The electron density values change when these factors change, but the general shape is similar.

### **3.3.1 Radio Signal Propagation**

The propagation speed of a radio signal changes as the signal travels through the varying ionosphere, with higher ionization levels increasing the phase velocity but decreasing the group velocity. This velocity change has the effect of refracting the signal path. The refractive index  $n$  of the ionosphere depends on the free-electron concentration and the wavelength of the signal according to the relationship [22:114]

$$n = \sqrt{1 - \frac{N_e q^2}{m \pi f^2}} = \sqrt{1 - \frac{8.1 \times 10^{-5} N_e}{f^2}} . \quad (4)$$

Here,  $N_e$  is the free electron density in  $\text{cm}^{-3}$ ,  $q$  is the magnitude of the charge on an electron in Coulombs,  $m$  is the electron mass in grams and  $f$  is the signal frequency in Hz ( $f$  in MHz for the far right-hand formula).

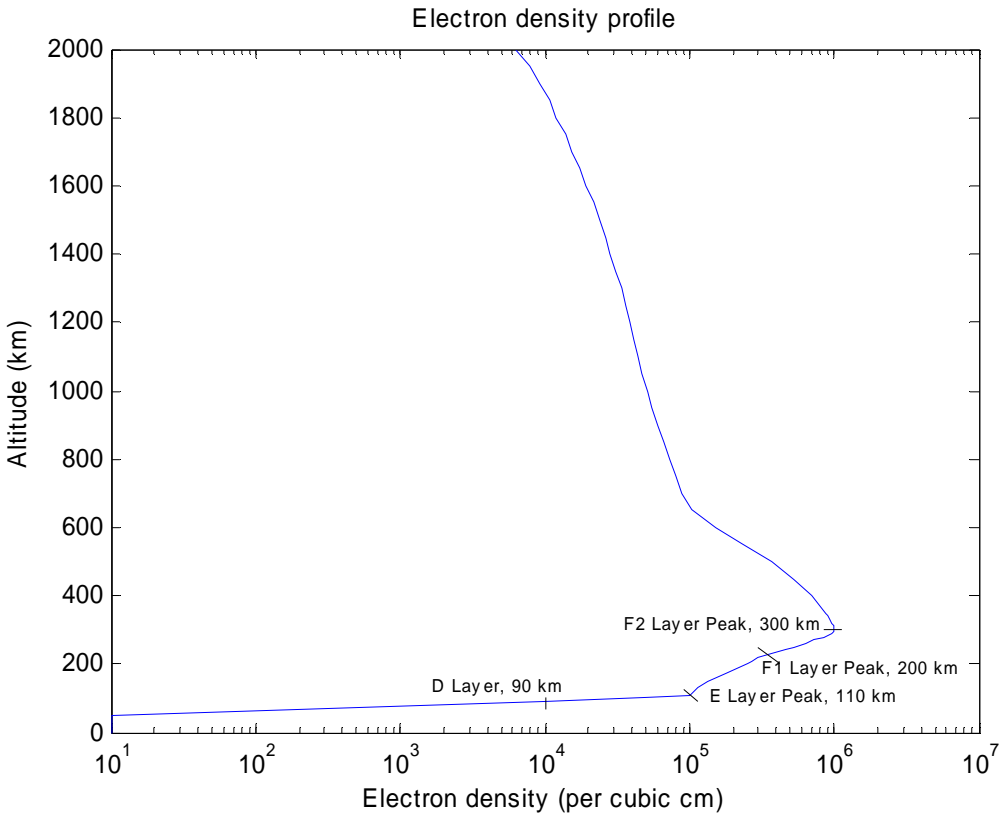


Figure 2. Electron density profile vs. altitude for daytime ionosphere under moderate solar activity.

If the electron density is sufficiently high, the number in the square root in (4) can go to zero. For a vertically incident wave, this situation occurs when

$$N_{ec} = \frac{f^2}{8.1 \times 10^{-5}} = 1.2 \times 10^{-4} f^2. \quad (5)$$

If this situation occurs, the signal is reflected back toward the ground and the value of  $N_e$  is known as the *critical density*. Similarly, for a given electron density the *critical frequency* is that frequency below which the signal is reflected, also known as the plasma frequency

$$f_c = 9 \times 10^{-3} \sqrt{N_e}. \quad (6)$$

When the signal is not vertically incident, the wave travels through more of the ionosphere at a given altitude and experiences more refraction. The critical frequency for a given  $N_e$  is lower than for a vertically incident wave. In this case, (5) and (6) must be modified to account for the angle of incidence  $\alpha$ . Equation (5) becomes

$$N_{e_c} = \frac{f^2}{8.1 \times 10^{-5}} = 1.2 \times 10^{-4} f^2 \cos^2 \alpha \quad (7)$$

and (6) is now

$$f_c = \frac{9 \times 10^{-3}}{\cos^2 \alpha} \sqrt{N_e}. \quad (8)$$

So for an ionospheric layer  $i$ , with electron density  $N_e$  the refractive index is

$$n_i = \sqrt{\frac{1 - 8.1 \times 10^{-5} N_e / f^2}{\cos^2 \alpha_i}}. \quad (9)$$

With the ionosphere sliced into spherical layers of constant  $N_e$ , this equation is applied to a small section of the ionosphere at a time. Using this approach, Snell's law of refraction

$$n_1 \sin \alpha_1 = n_2 \sin \alpha_2. \quad (10)$$

gives the ray path from one ionospheric layer to the next until the electron density reaches the critical density. Here,  $n_i$  is the refractive index of layer  $i$ ,  $\alpha_1$  is the angle of

incidence on the boundary between layers, and  $\alpha_2$  is the angle of refraction at which the ray enters the next layer.

Because of the spherical shape of the layers, the angle at which the ray path enters a layer is different to the angle of incidence on the next layer. The angles are related by

$$\sin(\alpha') = \frac{(y_1 + R_e)}{(y_2 + R_e)} \sin(\pi - \alpha) \quad (11)$$

where  $R_e$  is the radius of the earth and  $y_i$  is the altitude of the bottom of layer  $i$ . These angles are depicted in Figure 3.

Knowing the angles and layer thickness allows calculation of horizontal and vertical propagation distances. When this process is repeated for each layer of the ionosphere, the result is a curved path from the antenna. Depending on the frequency in use and the elevation angle on take-off, the ray may be returned to the ground or may escape into the upper atmosphere.

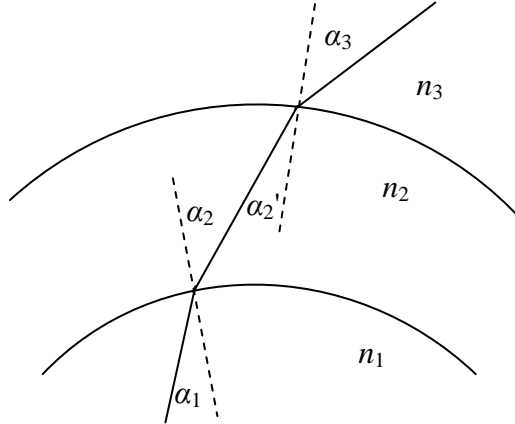


Figure 3. Angles of incidence and refraction in spherical layers. The path is refracted at the layer boundary, and meets the next layer at a different incidence angle due to the curvature.

Figure 4 shows a sample set of paths for four elevation angles:  $10^\circ$ ,  $25^\circ$ ,  $38^\circ$  and  $45^\circ$ , calculated at a frequency of 30 MHz. In comparison, the paths for the same angles at 15 MHz are shown in Figure 5.

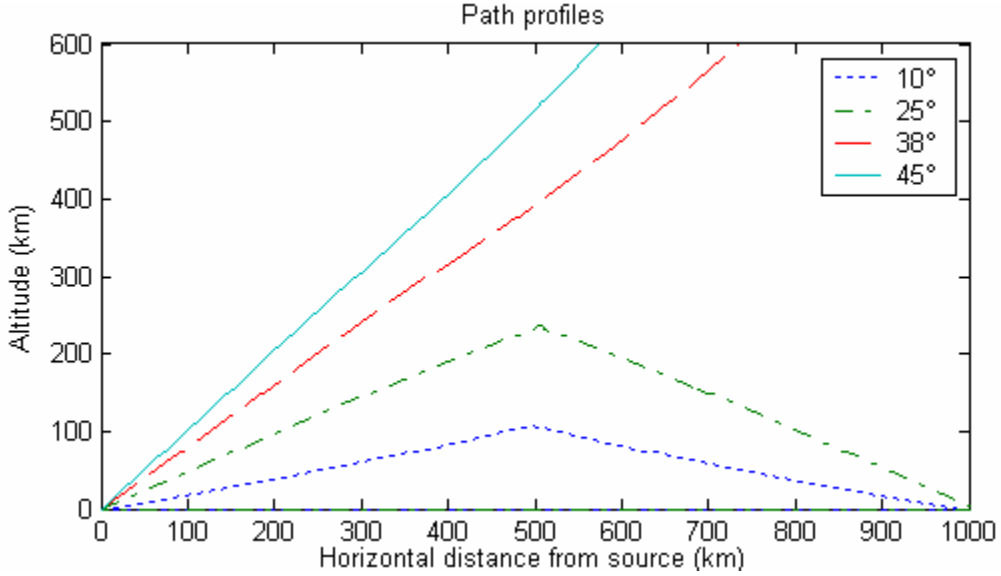


Figure 4. Path profiles for  $10^\circ$ ,  $25^\circ$ ,  $38^\circ$  and  $45^\circ$  elevation angles at  $f = 30$  MHz. The higher elevation angles penetrate the ionosphere.

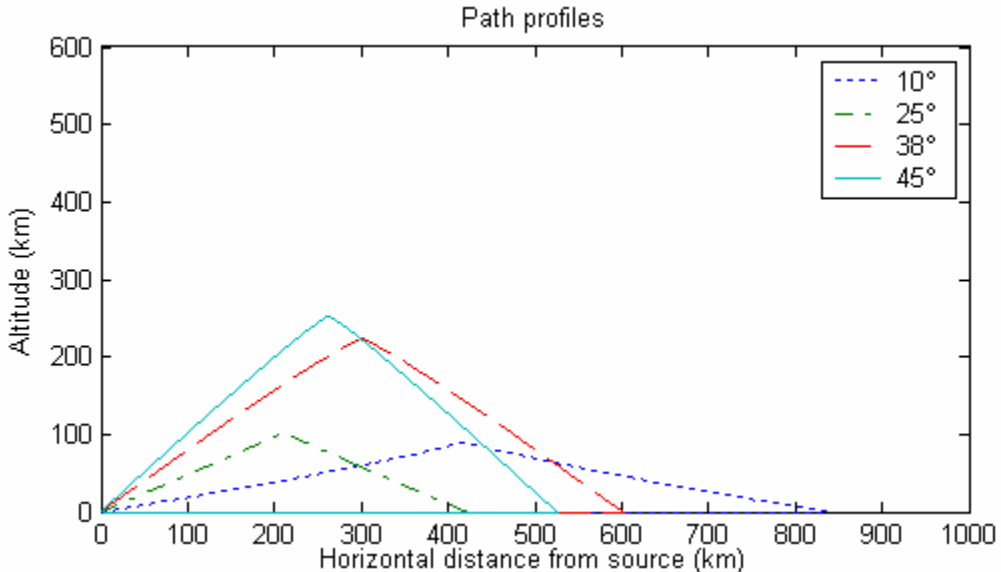


Figure 5. Path profiles for  $10^\circ$ ,  $25^\circ$ ,  $38^\circ$  and  $45^\circ$  elevation angles at  $f = 15$  MHz. Here, all radiation is returned to earth.

### **3.3.2 Cutoff Angles**

Higher frequencies experience less refraction, and so are more likely to pass through the ionosphere. The structure of the ionosphere means that for a given frequency there is a cutoff angle below which all paths return to the ground. Figure 6 shows the complete set of paths for elevation angles from 1 to 90°, at 1° increments. For the electron density profile in Figure 2 and a frequency of 30 MHz, the cutoff angle is 35.4°. In this figure, the paths have some distortion as they are calculated over a spherical earth, while the plots are over a flat axis.

This cutoff angle determines the radar's space coverage region. Space targets below the cutoff angle are obscured by the ionosphere. Higher frequencies have a lower cutoff angle, so choosing a high frequency maximizes the coverage region. The maximum frequency for the JORN system is 32 MHz, and this model uses 30 MHz for all calculations. This frequency limit is a major limitation on the performance of an OTHR for space surveillance.

### **3.3.3 Path Lengths to Ground**

Figure 6 also reveals the layered structure of the ionosphere, which is further visible in Figure 7. This plot breaks the paths up into groups, known as modes, which are returned to earth by the three principal ionospheric layers. The F2 layer mode group is notable because the ground patches illuminated are compressed more tightly than would be seen if the effect was a straight reflection from the ionosphere. This effect is important when considering the radar return from the ground.

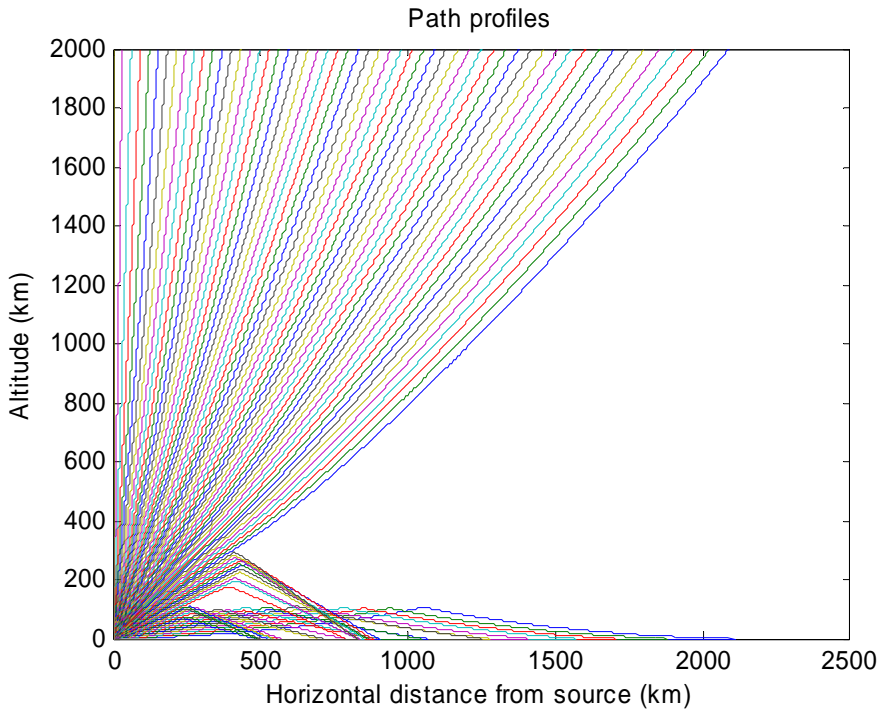


Figure 6. Path profiles for elevation angles from 1-90°.

The radar sees the ground as *clutter*—unwanted interference that can mask a target at the same range. The path lengths to the ground determine which part of the clutter the target must compete with. The strength of the clutter return is also dependent on the range, as will be explained in the next chapter.

### 3.4 Summary

The ionosphere restricts radar coverage for space surveillance to above a cutoff angle, dependent on ionospheric density and operating frequency. A higher frequency gives a lower cutoff angle and a larger coverage region, but OTHR systems are limited to the HF band and have an upper frequency limit of 28-32 MHz.

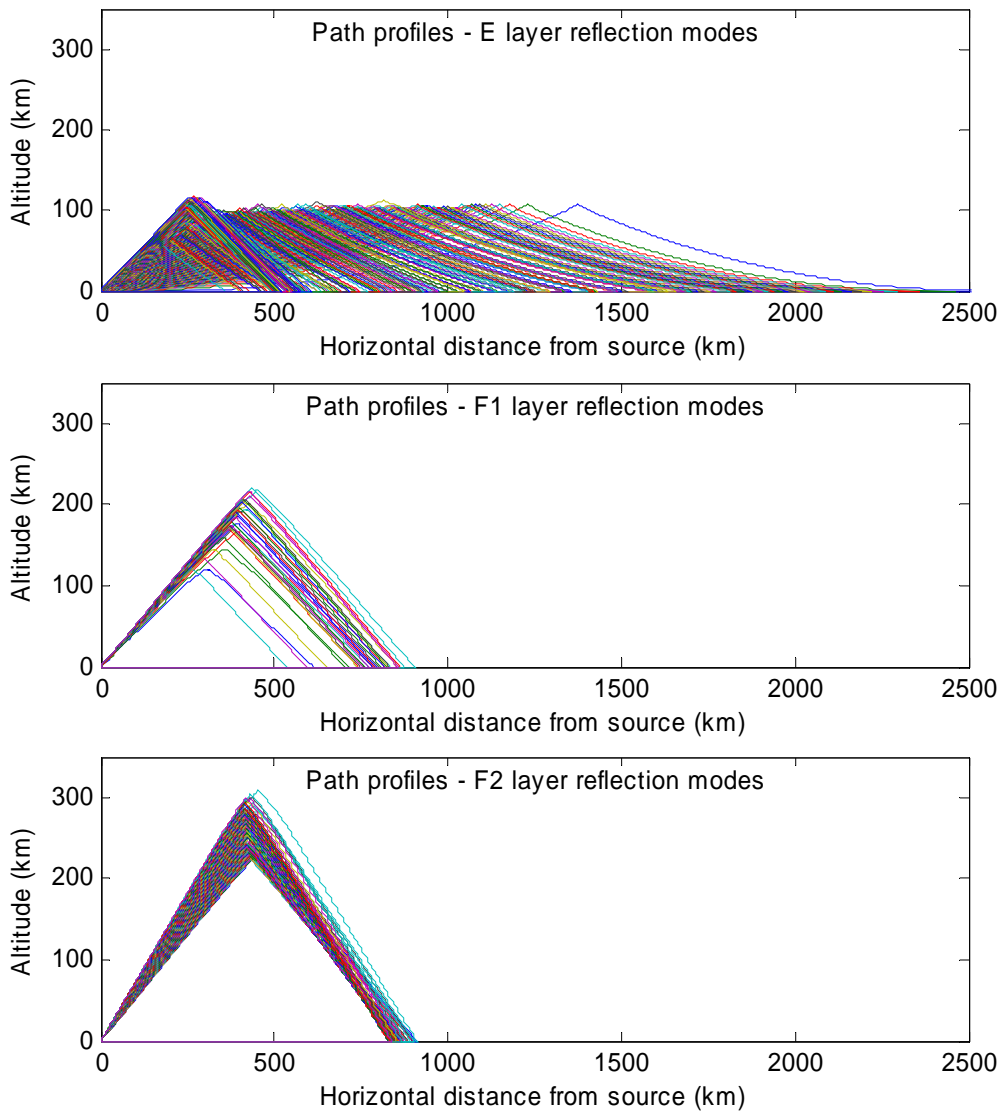


Figure 7. Path plots of E, F1 and F2 layer propagation modes. The layer modes correspond to refraction at the different ionospheric layers

Knowing the path that a ray takes through the atmosphere allows calculation of its propagation distance, either to the ground, or to a target in the upper atmosphere. These propagation distances are necessary for consideration of the radar operations, as explained in Chapter 4. Another important factor is the distribution or spreading of power

as the signal propagates. The ionospheric model, along with a model of the antenna, accounts for this power distribution.

## IV. Radar Model

### 4.1 Chapter Overview

This chapter explains the model used to describe the radar, its antenna, and its processing and detection. There are two main radar model components: the antenna and the clutter environment. The antenna model, together with the ionospheric model from the previous chapter, describes the power spreading from the radar transmitter. The ionospheric model also gives the path length to the ground. The path lengths determine the sections of ground clutter, known as *clutter rings*, that compete with a target.

The power spreading and path lengths are then used in the clutter model to calculate the levels of interference returned by the clutter. These clutter levels dictate minimum characteristics of a target to allow detection.

### 4.2 General Considerations

The large differences in path lengths for different elevation angles at the antenna mean that the choice of radar operating parameters is critical. The radar pulse repetition frequency (PRF)  $f_p$  and the coherent integration period, or number of pulses integrated, have large effects on the radar performance. The impact of changes in these parameters is explained below.

Several radar properties influence its performance. The most important of these for this thesis are the unambiguous range  $R_u$ , which is the longest target range the system can resolve, and the Doppler space, which is the extent of target Doppler frequencies the system can determine. The unambiguous range and the Doppler space are competing

requirements, requiring a tradeoff. Interpulse coding is a common technique for improving the available Doppler space without decreasing the unambiguous range. The target characteristics mean that the OTHR system requires interpulse coding to detect real targets. These properties are explained in more detail in this chapter. Interpulse coding is not modeled directly, but its potential effects are indicated.

Although most OTHR systems are bistatic, with transmitters and receivers separated by tens of kilometers, the system is modeled as monostatic. The simplifications introduced in the ionospheric model mean this choice has little impact on the model performance, but greatly simplifies the problem geometry and calculations.

### 4.3 Antenna Model

Each OTHR antenna is a long array of monopoles above a large artificial ground plane with a reflecting screen to reduce radiation in the backward direction. Mathematically, an OTHR antenna array can be described as a finite-length monopole with a reflected component to account for the influence of the ground and an array factor to account for the directionality provided by the array.

#### 4.3.1 Dipole Pattern

For a thin dipole of finite length  $l$ , the radiation pattern is given by [1:153]

$$g_d(\alpha) = z_0 \frac{I_0}{8\pi^2} \left[ \frac{\cos\left(\frac{kl}{2}\cos(\alpha)\right) - \cos\left(\frac{kl}{2}\right)}{\sin(\alpha)} \right]^2, \quad (12)$$

where  $g_d(\alpha)$  is the power pattern in the direction of  $\alpha$ , the declination from vertical,  $z_0$  is the impedance of free space,  $I_0$  is the reference intensity (or current for a power pattern), and  $k = 2\pi / \lambda$  is the wave number. Declination from vertical is more commonly used in antenna theory and so retained in these equations. The power pattern for a dipole is constant in  $\phi$ , the azimuth angle. The thin wire approximation is valid for thicknesses  $\leq \lambda/100$  [14:177]. Given the operating wavelength is at least 10.0 m and the thickness of the OTHR antenna elements is approximately 5.0 cm, the approximation is valid.

#### **4.3.2 Monopole Pattern**

The antenna elements are actually monopoles above an imperfect ground plane. *Image Theory* allows a monopole element near a conducting surface to be treated as a dipole with a virtual source introduced to account for reflections. Figure 8 shows how the direct and reflected contributions combine.

Although this is a reflection situation, the ground does not act as a specular reflector. Instead, a form of Snell's law relates the incident and reflected angles for the reflected component, so that

$$\gamma_0 \sin \alpha_i = \gamma_1 \sin \alpha_r . \quad (13)$$

Here,  $\gamma_0 = jk_0$  is the propagation constant for free space (air), and  $k_0$  is the phase constant for free space, which is equal to 1. The propagation constant for the ground is  $\gamma_1 = \varsigma_1 + jk_1$ , where  $\varsigma_1$  is the attenuation constant and  $k_1$  is the phase constant for the ground. As the ground approaches an ideal reflector,  $\varsigma_1$  approaches 0 and  $k_1$  approaches -1.

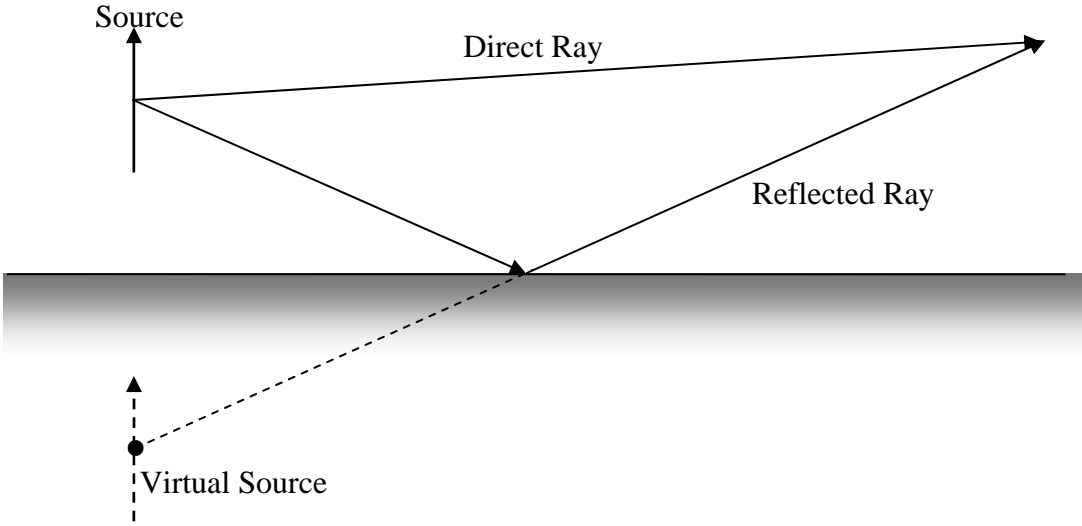


Figure 8. Combination of direct and reflected rays. The reflected ray is equivalent to a ray from a virtual source or *image* of the real antenna.

The ‘far–field’ or Fraunhofer region of an antenna begins at a distance such that the radiation pattern at a given angle is independent of distance. The angles  $\alpha_i$  and  $\alpha_r$ , for far–field observations, are shown in Figure 9.

The dipole power pattern is multiplied by a reflectivity term to account for the ground reflection, giving the gain pattern for a monopole  $g_m(\alpha)$  [1:183]

$$g_m(\alpha) = g_d(\alpha) \left( e^{jkh \cos \alpha} + R_v e^{-jkh \cos \alpha} \right) \text{ defined for } 0 \leq \alpha < \pi / 2, \quad (14)$$

where  $h$  is the element base height above the ground and the reflectivity factor  $R_v$  is

$$R_v = \frac{-z_0 \cos \alpha_i + z_1 \cos \alpha_r}{z_0 \cos \alpha_i + z_1 \cos \alpha_r}. \quad (15)$$

Here,  $z_0$  and  $z_1$  are the impedance of free space and the ground, respectively, given by

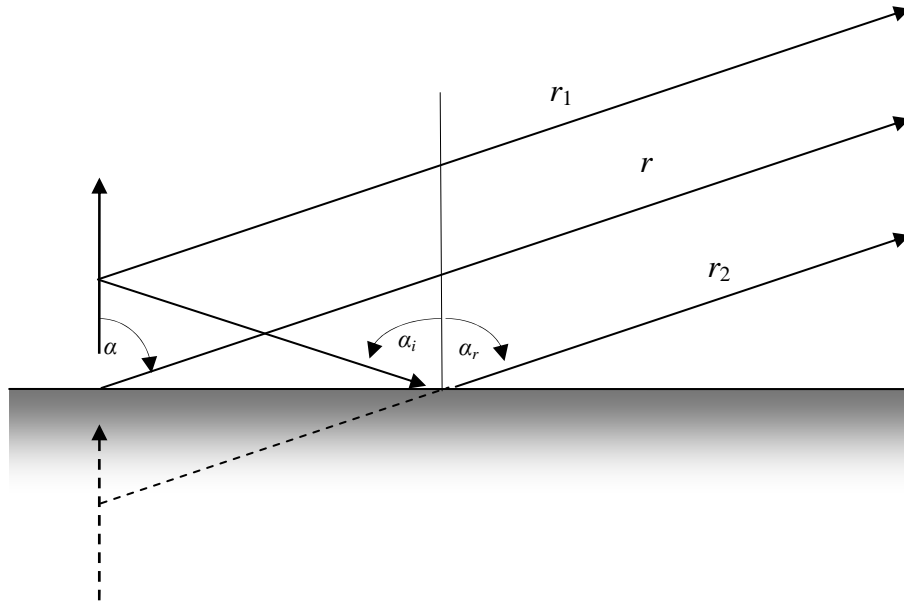


Figure 9. Angles of incident and reflected rays. The electrical properties of the ground means that it does not act as a specular reflector. The angles  $\alpha_i$  and  $\alpha_r$  are related by (13).

$$z_0 = \sqrt{\frac{\mu_0}{\epsilon_0}} , \quad (16)$$

and

$$z_1 = \sqrt{\frac{j\omega\mu_1}{\sigma_1 + j\omega\epsilon_1}} , \quad (17)$$

where  $\omega$  is the angular frequency of the emitted signal,  $\mu$ ,  $\epsilon$  and  $\sigma$  are permeability, permittivity and attenuation, respectively, and the subscript 0 denotes free space while subscript 1 denotes the ground.

The resultant element gain pattern is shown in polar form in Figure 10, and in Cartesian form in Figure 11, where  $\alpha$  is defined as  $0^\circ$  at vertical. Only the first quadrant is shown, although the pattern is constant in azimuth (about the vertical) and repeats in the second quadrant. Figure 12 shows more detail of the main beam and principal sidelobes.

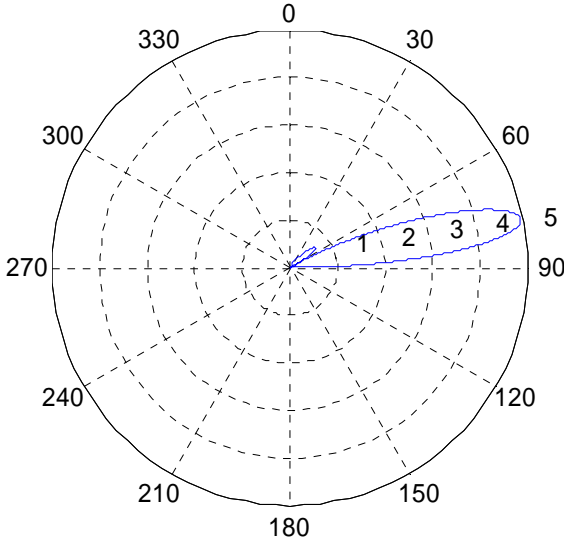


Figure 10. Polar view of element gain pattern,  $f = 30$  MHz. The main lobe is visible at  $12^\circ$  elevation, and the principal sidelobe is at  $38^\circ$ .

The main beam is centered on  $78^\circ$  declination, or  $12^\circ$  elevation, and the principle sidelobe is centered on  $52^\circ$  declination, or  $38^\circ$  elevation.

#### 4.3.3 Array Factor

To obtain the radiation pattern for the whole array, the element pattern  $g_m(\theta)$  of (14) is multiplied by an array factor  $AF$  given by

$$AF(\phi) = e^{j[(N-1)/2]\phi} \left[ \frac{\sin(N\phi/2)}{\sin(\phi/2)} \right], \quad (18)$$

where  $\phi = kd \cos(\phi) + \beta$  and  $N$  is the number of uniformly spaced antenna elements.

Here,  $k=2\pi/\lambda$  is the wave number,  $d$  is the separation between array elements,  $\phi$  is the azimuth angle measured with respect to the array axis and  $\beta$  is the angular phase separation or delay between elements. For the model,  $\beta$  is assumed uniform and zero,

although for a real system this phase separation could be altered to steer the main beam and nulls in desired directions.

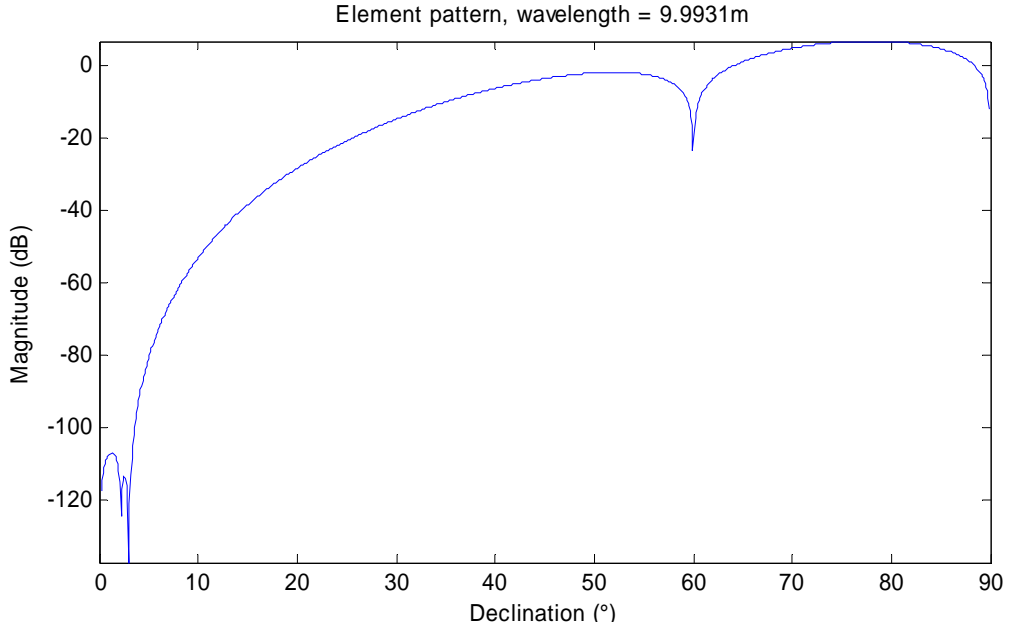


Figure 11. Monopole element pattern for  $f = 30\text{MHz}$ . The main lobe is at  $78^\circ$  declination.

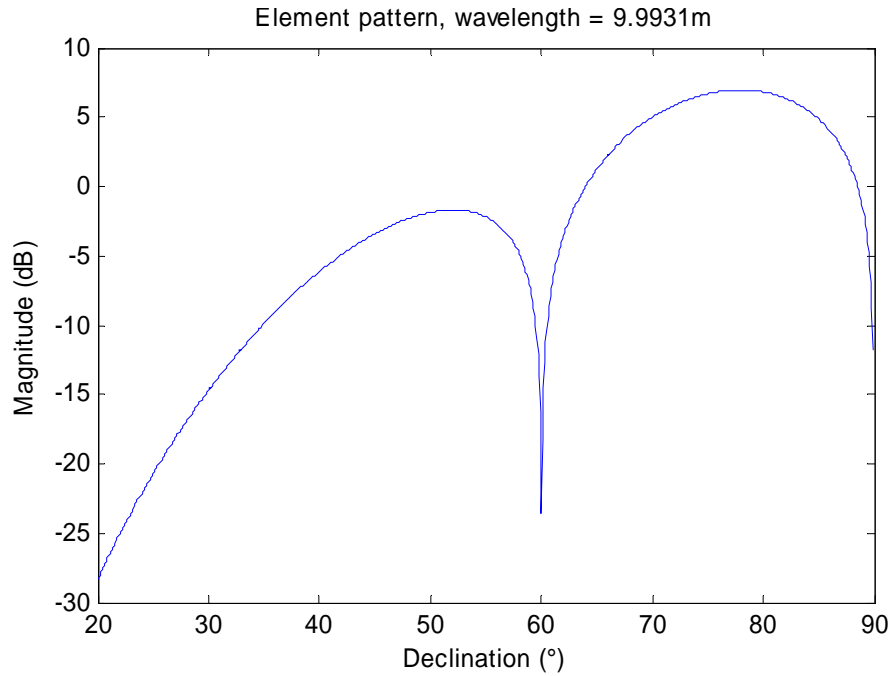


Figure 12. Detail of monopole element pattern,  $f = 30\text{ MHz}$ . The main lobe peak is at  $78^\circ$  declination and the sidelobe peak is  $52^\circ$ . The null occurs at  $60^\circ$ .

Applying L'Hopital's rule to (18), the array factor peak occurs at  $\phi = 90^\circ$ , where the magnitude limits to  $N$ , the number of elements in the array. This peak is the maximum array factor value. For the antenna configuration considered,  $N = 82$ .

The real antenna array consists of one row of active elements with a reflecting screen to reduce backlobes. This model simplifies this construction and scales the back lobes by 20 dB, using a scaling factor  $B$  defined as

$$B = \begin{cases} 1, & 0 < \phi < 180 \\ 0.01, & 180 \leq \phi \leq 360. \end{cases} \quad (19)$$

Figure 13 shows the array factor in Cartesian coordinates with the backlobe attenuation applied.

The main lobe height and the narrowness of the main beam and sidelobes obscure the sidelobe structure. Figure 14 shows this structure in more detail, from  $70$  to  $110^\circ$  azimuth. This figure shows the very narrow main beam and side lobes. As a result, the antenna pattern is strongly directional in azimuth. However, the one-dimensional antenna array has no effect on the pattern shape in elevation.

#### **4.3.4 Overall Antenna Pattern**

The complete array pattern  $G(\alpha, \phi)$  is given by multiplying the element gain  $g_m(\alpha)$  by the array factor  $AF(\phi)$  and the backlobe attenuation:

$$G(\alpha, \phi) = g_m(\alpha) AF(\phi) B. \quad (20)$$

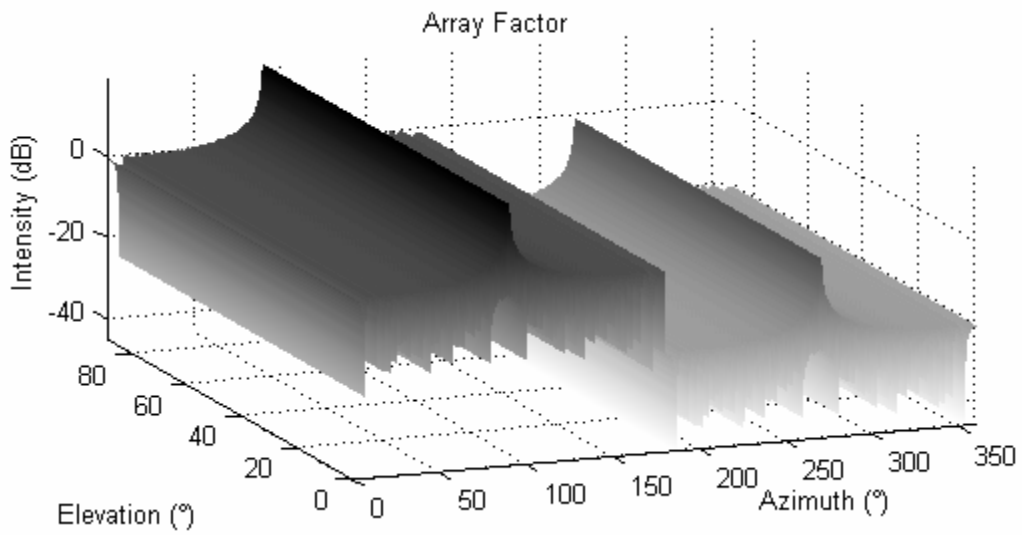


Figure 13. Array factor,  $f = 30$  MHz. The backlobe attenuation is visible as a 20 dB drop in gain for azimuth greater than  $180^\circ$ .

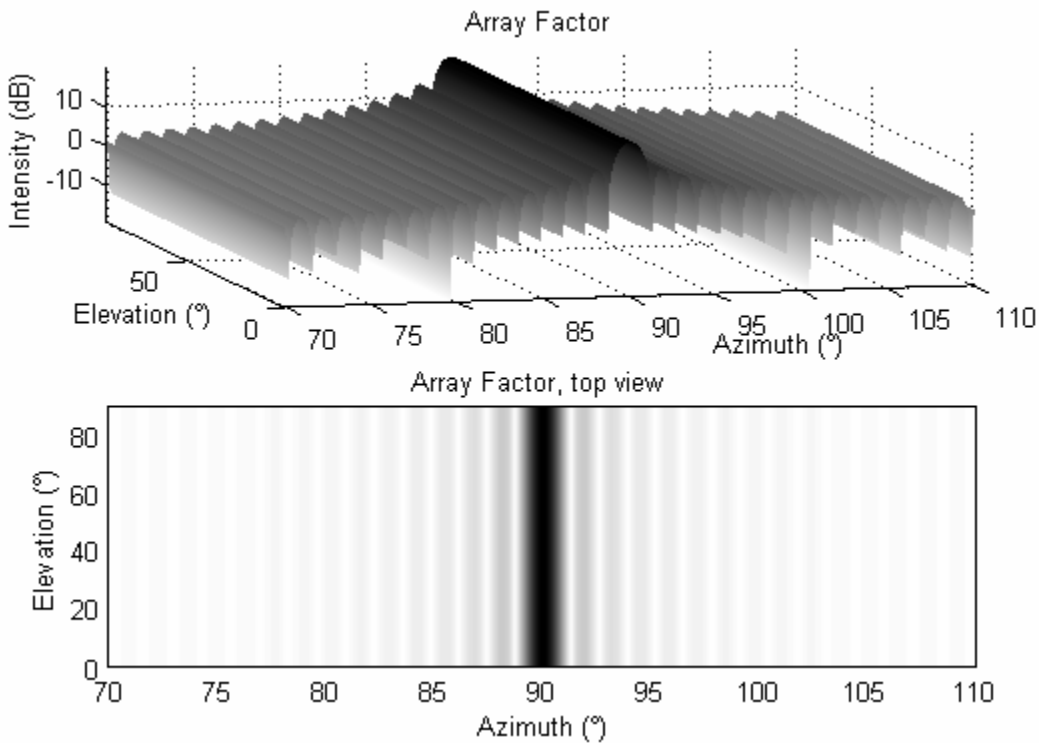


Figure 14. Main lobe of array factor,  $f = 30$  MHz. Darker areas represent higher intensity. The main lobe is centered on  $90^\circ$  azimuth.

Figure 15 shows the resultant pattern for the entire antenna. Again, the sidelobes in azimuth are obscured, so Figure 16 shows the main lobe and surrounding details while Figure 17 shows a top view of the same region. The important features are the main beam with gain 26 dB centered on  $12^\circ$  elevation and  $90^\circ$  azimuth and the elevation sidelobe with gain 17 dB centered on  $38^\circ$  elevation and  $90^\circ$  azimuth.

The elevation beamwidth is entirely dependent on the element length in relation to the operating wavelength, while the azimuth beamwidth depends primarily on the number of array elements. For the receive array of  $N = 82$  elements, the beam is very narrow in azimuth, with a half-power beamwidth of  $1.56^\circ$ . Although the beam can be steered, the beam is centered on boresight for this model and the half-power points are at  $89.22^\circ$  and  $90.78^\circ$  azimuth. In elevation, the half-power points of the main lobe are at  $68.2^\circ$  and

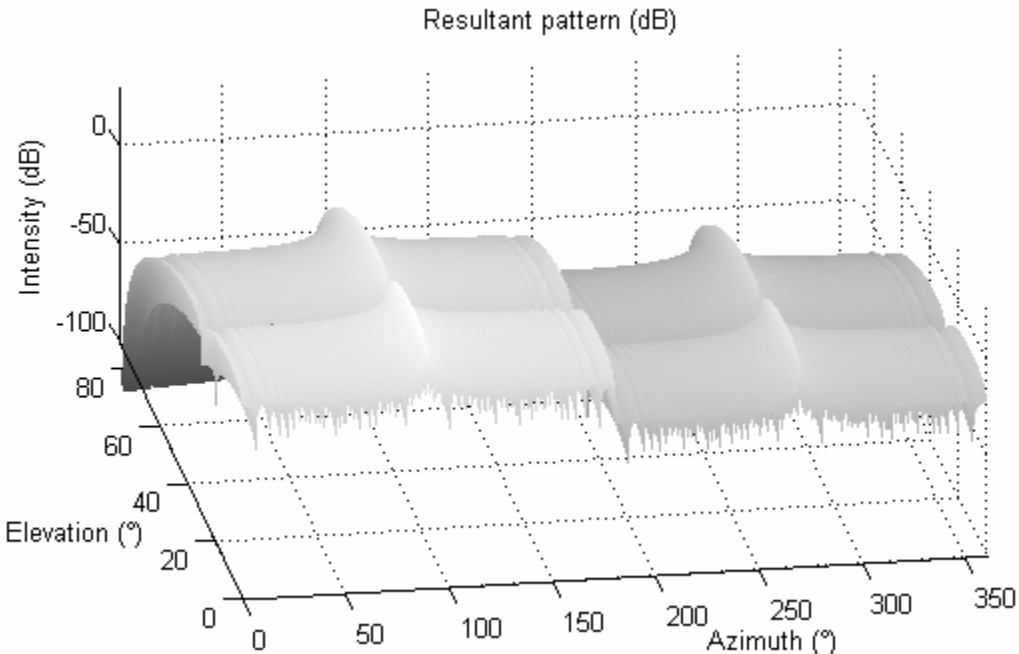


Figure 15. Resultant antenna pattern,  $f = 30$  MHz. Again, the pattern shows the 20 dB backlobe attenuation, with the main lobe centered at  $90^\circ$  azimuth.

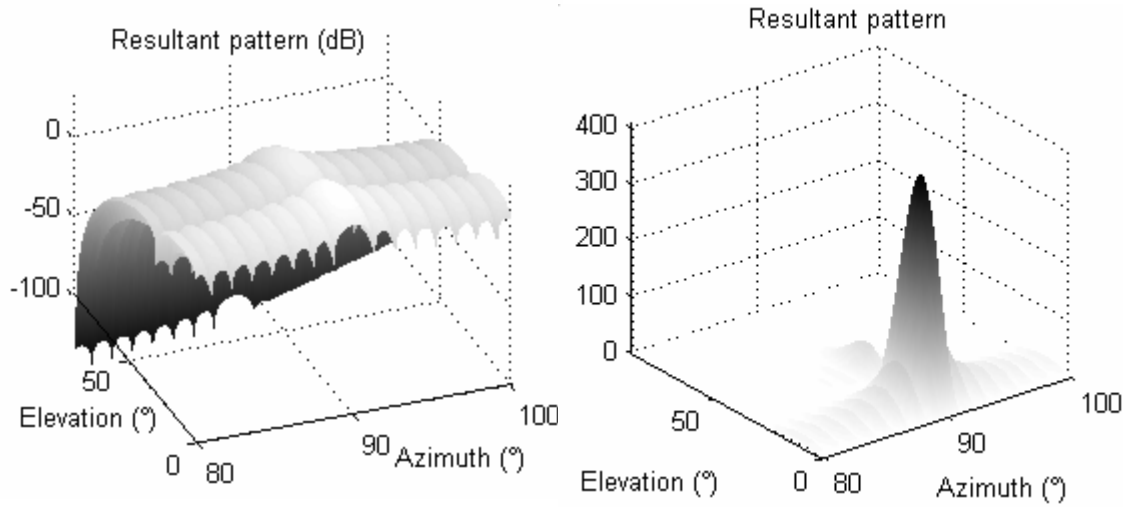


Figure 16. Main lobe and principle sidelobes of antenna pattern,  $f = 30$  MHz. The left hand figure shows the pattern in dB while the right hand figure shows the pattern in absolute numbers.

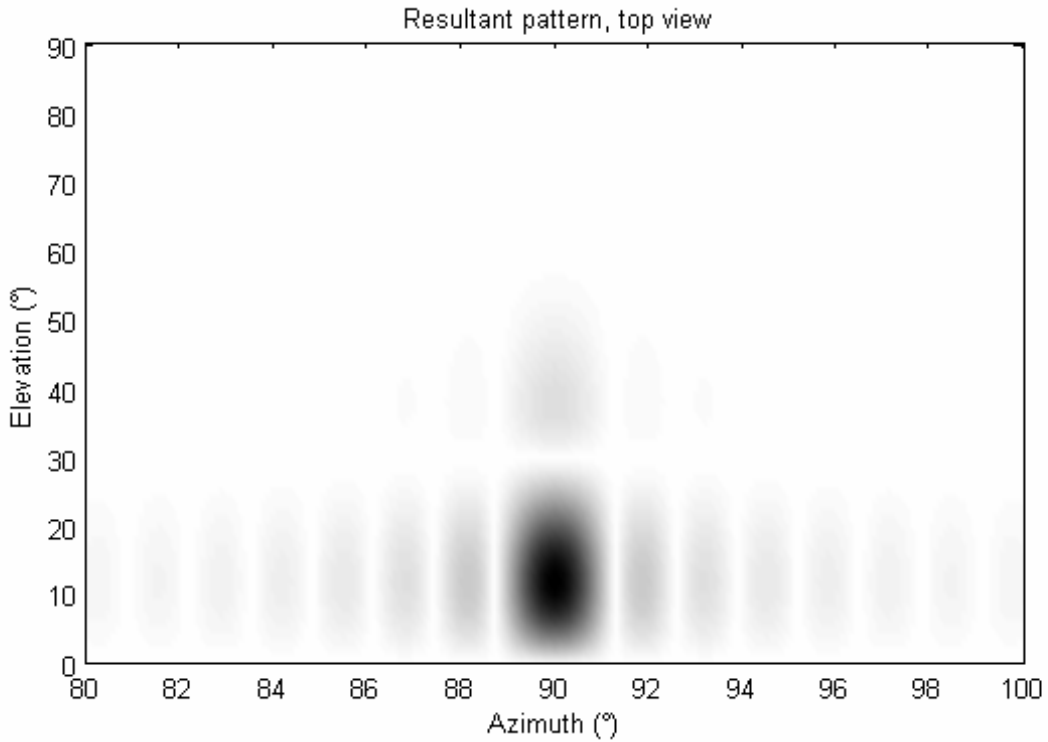


Figure 17. Top view of main lobe showing zeros between lobes,  $f = 30$  MHz, with the scale in azimuth magnified to show detail. Darker areas represent higher antenna gain. The main lobe is the dark area in the bottom-center (azimuth =  $90^\circ$ , elevation =  $12^\circ$ ) and the elevation sidelobe is immediately above this (azimuth =  $90^\circ$ , elevation =  $38^\circ$ ).

86.1° declination (21.8° and 3.9° elevation) at 30 MHz, giving a 17.9° beamwidth. These model results compare closely with published figures of 14° elevation and 1.25° azimuth beam widths, and 24 dB of peak antenna gain [9; 17]. These half-power points can be seen in the cross-sections in Figure 18 and Figure 19.

The sidelobe in Figure 19 is of interest as this contains the energy that penetrates the ionosphere, and so will illuminate any space-based target. When combined with the path plots from the ionospheric model, the antenna model gives a useful illustration of the radiated power distribution as shown in Figure 20. The ionosphere passes radiation at 35.5° or more elevation, while radiation at less than 35.5° elevation is refracted back to earth. This cut-off angle varies with operating frequency and ionospheric conditions but under the conditions modeled is in the elevation sidelobe. During night-time ionospheric

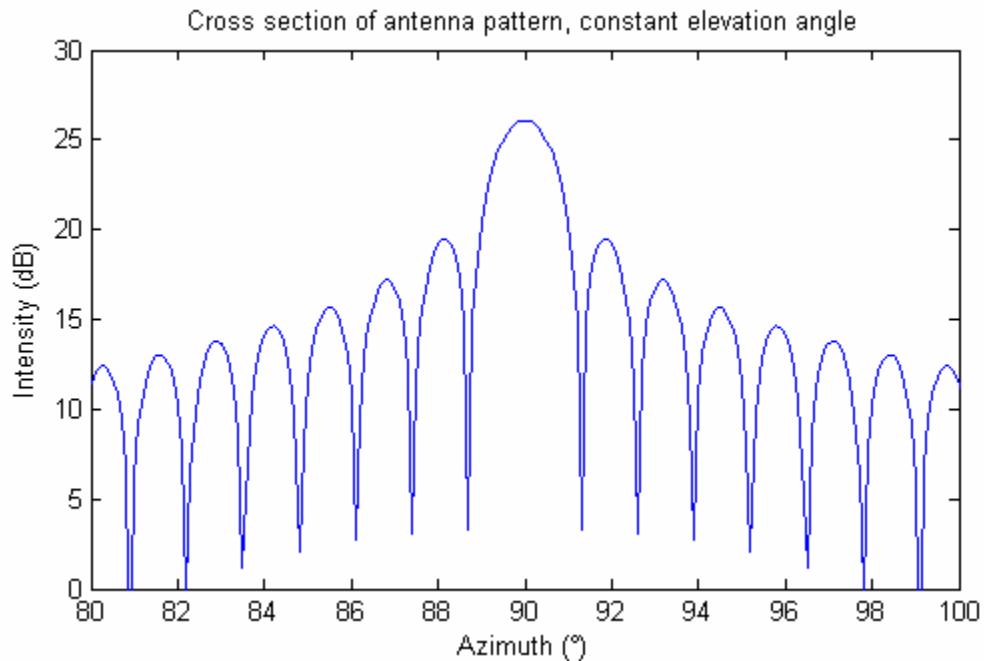


Figure 18. Cross sectional view of main lobe for 12° elevation angle, at main lobe peak, for  $f = 30$  MHz.

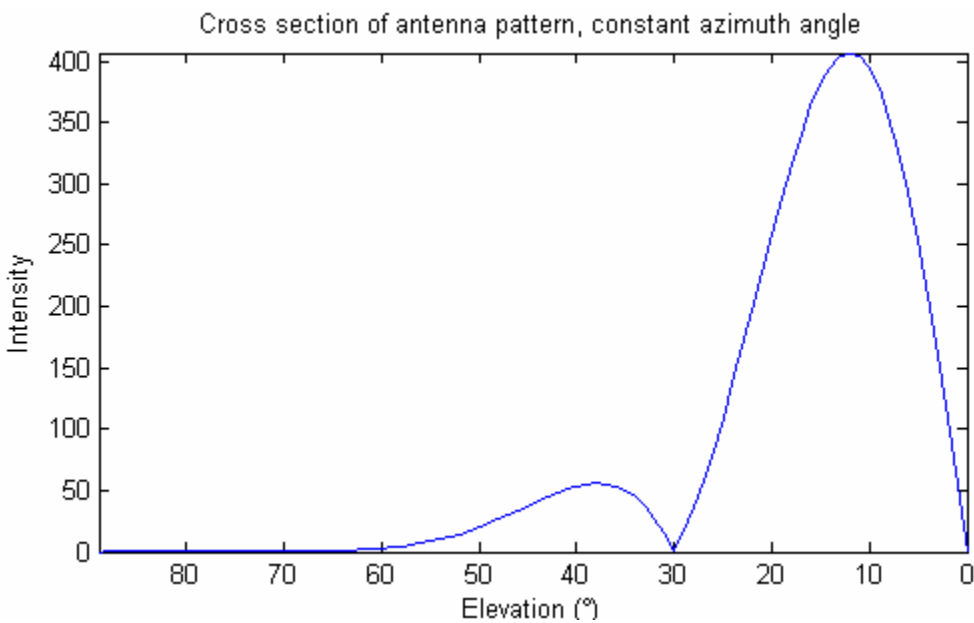


Figure 19. Cross sectional view of antenna pattern for  $90^\circ$  azimuth angle, at main lobe peak, for  $f = 30$  MHz.

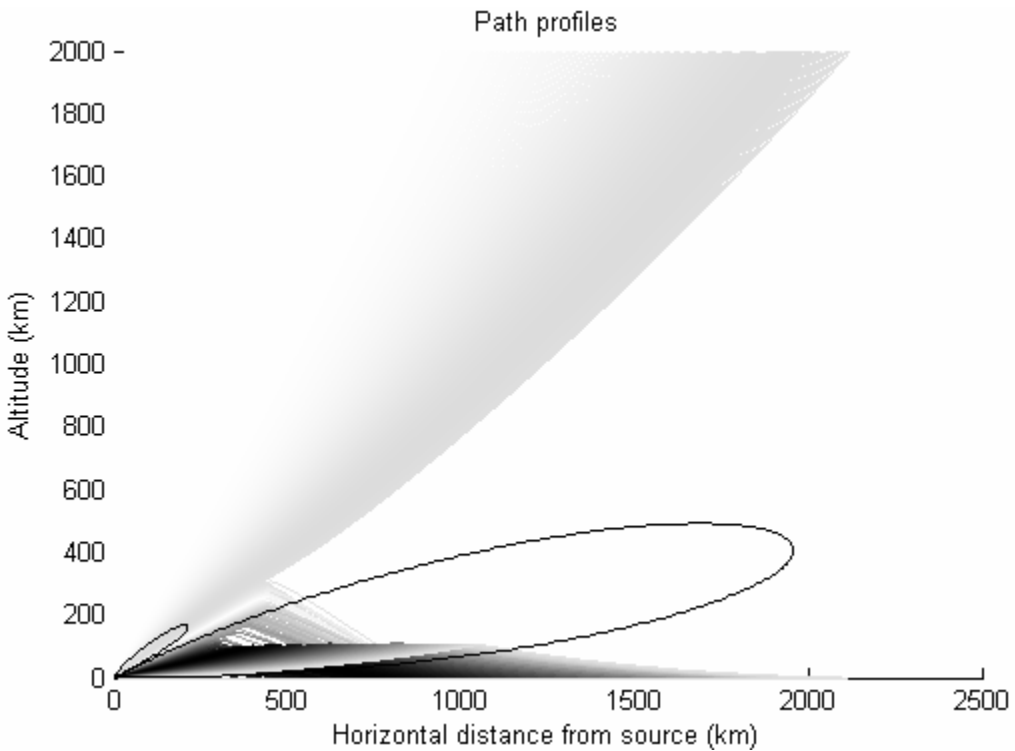


Figure 20. Radiated power distribution with the antenna pattern superimposed. Darker colors represent higher power levels. The  $35.5^\circ$  cutoff angle is clearly visible.

conditions this cutoff angle is lower, giving lower clutter returns; however, the conditions modeled show typical performance.

#### 4.4 Thermal Noise

Although thermal noise is present and provides an absolute upper limit on system performance, the high transmit power and large clutter patches overwhelm the noise in almost all situations. Still, the noise is modeled as a white Gaussian source with an average power  $\sigma^2$  given by

$$\sigma^2 = kTB_n , \quad (21)$$

where  $k$  is Boltzmann's constant,  $T$  is the system noise temperature and  $B_n$  is the receiver noise bandwidth. This work uses values of  $T = 300$  K and  $B_n = 50$  kHz, a conservative assumption.

To allow statistical comparison, noise power is represented in a covariance matrix  $\mathbf{R}_n$  given by

$$\mathbf{R}_n = kTB_n \mathbf{I}_{MNP} , \quad (22)$$

where  $M$  is the number of radar pulses integrated,  $N$  and  $P$  are the number of elements in the  $N \times P$  antenna array and  $\mathbf{I}_{MNP}$  is an identity matrix of size  $MNP$ . The OTHR uses a one-dimensional array, so  $P = 1$ .

The noise covariance matrix comes from a snapshot  $\chi_n$  which is a vector of length  $MNP$  and contains the noise voltage seen at each antenna element so that  $\chi[1]$  is the return at the first element from the first pulse,  $\chi[2]$  is the return at the second element

from the first pulse,  $\chi[N+1]$  is the return at the first element from the second pulse, up to  $\chi[MNP]$ , the return at the last element for the last pulse.

The covariance matrix is then the expected value of the product of  $\chi_n$  with its conjugate-transpose, equivalent to

$$\mathbf{R}_n = \mathbb{E}\{\chi_n \chi_n^H\}, \quad (23)$$

and is a matrix of zero mean and standard deviation of  $kTB_n$ .

## 4.5 Clutter Model

The high transmit power levels used in the OTHR mean the returns from ground patches, or clutter, illuminated by the radar are at a far higher level than thermal noise. To characterize the clutter, the ground is broken into rings of constant range with each ring then divided up in azimuth. The model here is based on Hale [10], which draws from Ward [25]. A key difference is that these models are developed for airborne radar, whereas the model implemented for this thesis is for a ground-based OTHR.

### 4.5.1 Geometry

The ground clutter is divided into rings of constant range. The rings are seen at a range corresponding to the length of the refracted path  $R$ . Each ring has a width  $\Delta R$  corresponding to the projection of one radar pulse onto the ground. The projected length depends on the grazing angle  $\psi$  and is given by

$$\Delta R = \frac{c\tau_p}{2} \cos(\psi), \quad (24)$$

where  $c$  is the speed of light and  $\tau_p$  is the pulse width in seconds.

Each ring is then divided up into cells with a constant angular width  $\Delta\phi$ . The angular width is chosen small enough to reveal the antenna pattern details. The 82 element array, with  $1.5^\circ$  main lobe width, requires a fine azimuth resolution to capture the azimuth pattern peaks and nulls. For this model,  $\Delta\phi$  is chosen as  $0.1^\circ$ .

Figure 21 shows an example clutter ring, with its angles and path length. The range is determined from the ionospheric model. The grazing angle also follows from the ionospheric model; because the modeled ionosphere is spherically stratified, the angles on the ray's upward propagation path mirror the angles on the downward path. Hence, the grazing angle  $\psi$  at the clutter patch is the same as the elevation angle  $\theta$  from the antenna on takeoff.

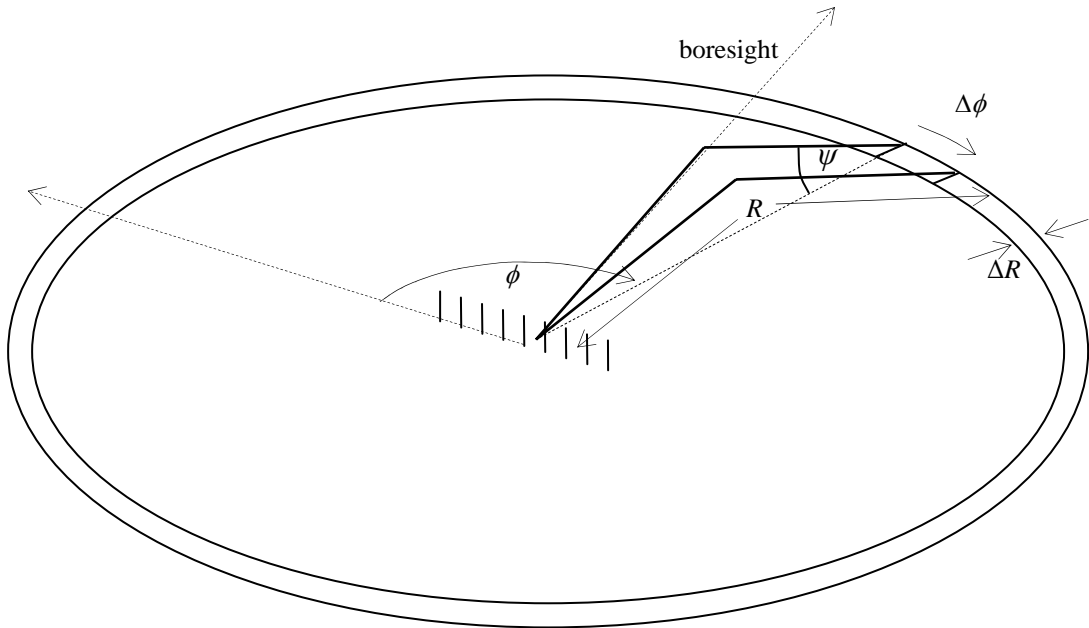


Figure 21. Clutter ring geometry, showing ranges and elevation/grazing ( $\psi$ ) and azimuth ( $\phi$ ) angles. The range  $R$  is the refracted path length given by the ionospheric model.

For the RCS of a particular clutter patch, one further factor is required to account for ground reflectivity. The reflectivity in the transmitter direction has been shown experimentally to be close to linear with the sine of the grazing angle, for small to medium grazing angles. This type of model is known as *constant gamma*, [13:126-128; 21:418-420] where

$$\gamma = \frac{\sigma^0}{\sin \psi} \quad (25)$$

and  $\sigma^0$  is the radar cross-section (RCS) per physical square meter of surface area. In the HF band, terrain features can be of a similar size to the wavelength resulting in Bragg scattering, so  $\gamma$  varies considerably with variations in the terrain. For smooth land at HF wavelengths,  $\gamma$  is  $5 \times 10^{-4}$  [13:128] or -33 dB. The RCS of the clutter cell,  $\sigma_c$ , is then

$$\sigma_c = \frac{(2R - \Delta R)}{2} \Delta R \Delta \phi \sigma^0. \quad (26)$$

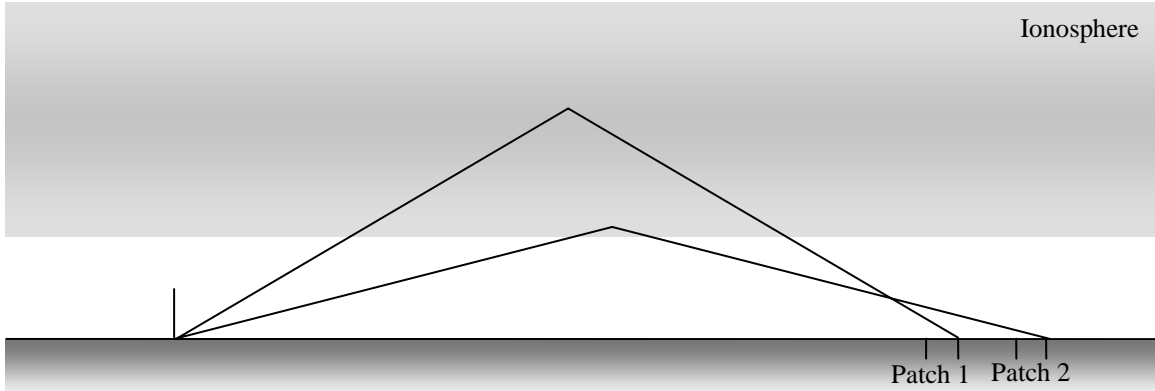


Figure 22. Example of two different clutter patches at the same path length. Each patch is part of a ring with that apparent range and the two rings add to provide the interference for the same target range.

The path profile complexities may mean that more than one clutter ring is seen at the same apparent range, as illustrated in Figure 22. While this model treats the ground as homogeneous in terms of its reflectivity characteristics, the clutter patches at different ranges have different sizes and grazing angles and each range must be treated separately.

#### 4.5.2 Range to Clutter Rings

Because of path length variations, the range to a clutter ring is not a single-valued function of elevation angle. The plot in Figure 23 shows the variation in path lengths with elevation angles, as traced through the ionosphere using the model from Chapter 3. There are marked discontinuities in the ranges, implying some clutter returns are missed with data this sparse. These regions with discontinuities correspond to angles where the path changes modes from E layer to F1 layer or from F1 layer to F2 layer.

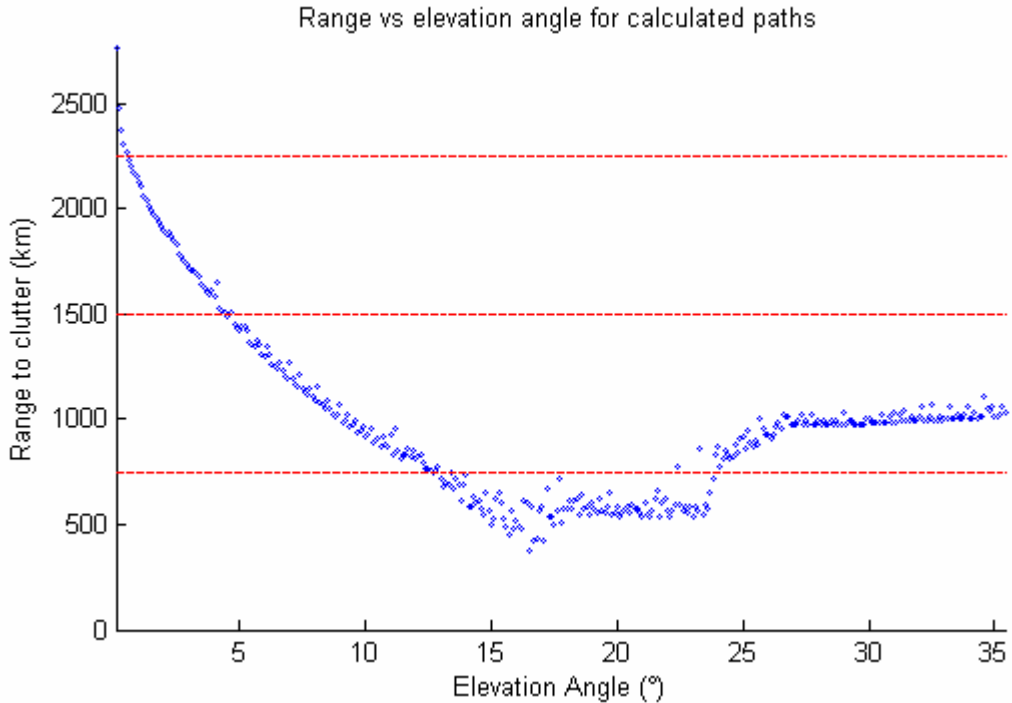


Figure 23. Range (path length) to clutter ring vs. elevation angle, with angles calculated at  $0.1^\circ$  intervals. The horizontal lines are at multiples of  $R_u$  for  $f_p = 200$  Hz.

The horizontal lines represent multiples of the unambiguous range  $R_u = c/2f_p$ , where  $c$  is the speed of light and  $f_p = 200$  Hz is the pulse repetition frequency (PRF). Clutter or targets of ranges  $R + nR_u$  are indistinguishable, for integer  $n$ , because the returns are *aliased* to the range  $R$ . This aliasing means the number of clutter rings in a given range cell depends on the pulse repetition frequency. In general, a lower value of  $f_p$  leads to less clutter rings aliased to a particular range cell. For  $f_p = 200$  Hz as shown, multiple clutter rings are seen at all target ranges.

To achieve continuity in the clutter rings, the range difference from one clutter ring to the next must be no more than the propagation distance of one radar pulse  $c\tau_p/2$ , where  $\tau_p$  is the pulse duration. This distance corresponds to the width of one *range bin*. For  $\tau_p = 20$   $\mu$ s, as modeled here, the range difference is 2.998 km.

Because of the computational load required to calculate path lengths and because the range is a multi-valued function of elevation angle, these ranges are interpolated for angular steps  $\Delta\theta$  of  $10^{-2}$  and  $10^{-3}$  $^\circ$ . A step size of  $10^{-3}$  $^\circ$  is required to give the required fidelity, such that the minimum difference from one calculated range to the next is no more than the range bin width.

Figure 24 shows the interpolated ranges at increments of  $10^{-2}$  $^\circ$ . Discontinuities in ranges are still noticeable at 17 to 18 $^\circ$  and 23 to 24 $^\circ$  elevation, with range differences of up to 30 km. These are more evident in Figure 25, where the ranges are now folded over, or aliased, at  $R_u$ , representing the apparent range as seen by the receiver. A target at any given range competes with the clutter returns corresponding to that range.

The clutter environment complexity is evident in Figure 26, which shows the number of clutter rings in each range bin. Range bins 75 to 90 and 180 to 210, corresponding to ranges off approximately 225 to 270 and 540 to 630 km, experience the strongest clutter returns due to the large number of clutter rings folded over into these range bins.

For a step size of  $10^{-3}$  $^{\circ}$ , the shapes of the plots are very similar, but the number of clutter rings is commensurately larger. Figure 27 shows the number of clutter rings in each range bin for this step size. The number of clutter rings shown is *not* indicative of the actual clutter fold-over. They are an artifact of the interpolation that is corrected next.

The smaller step size gives many clutter rings of *adjacent* elevation angles with path lengths in the same range bin. To avoid potential double counting of clutter returns,

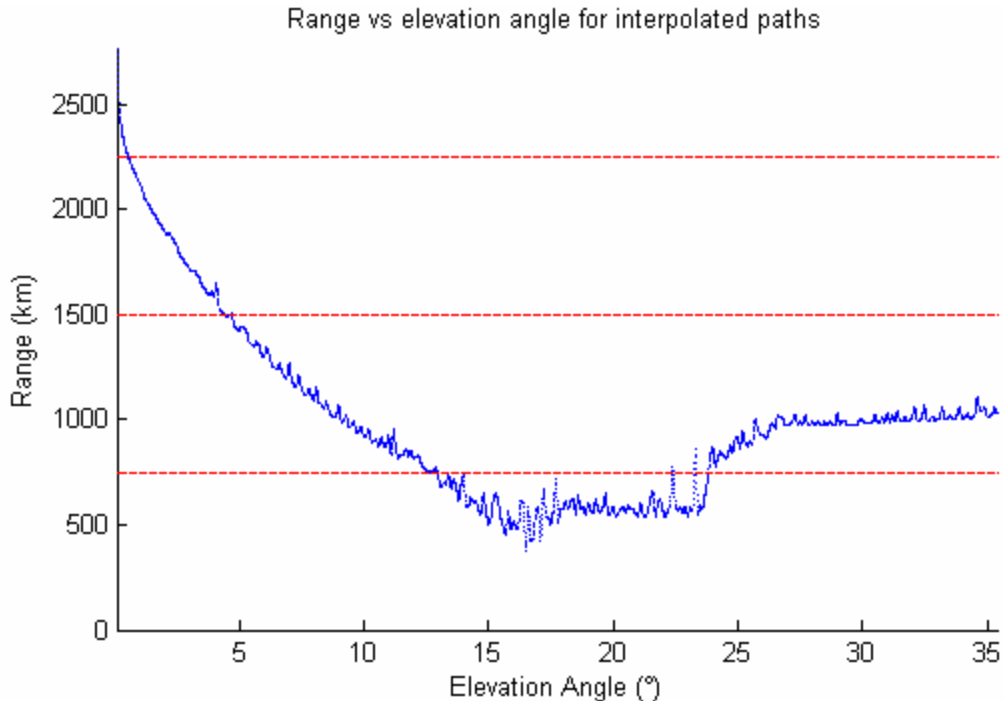


Figure 24. Range (path length) to clutter ring vs. elevation angle of interpolated paths, at increments of  $10^{-2}$  $^{\circ}$ . The horizontal lines are at multiples of  $R_u$  for  $f_p = 200$  Hz.

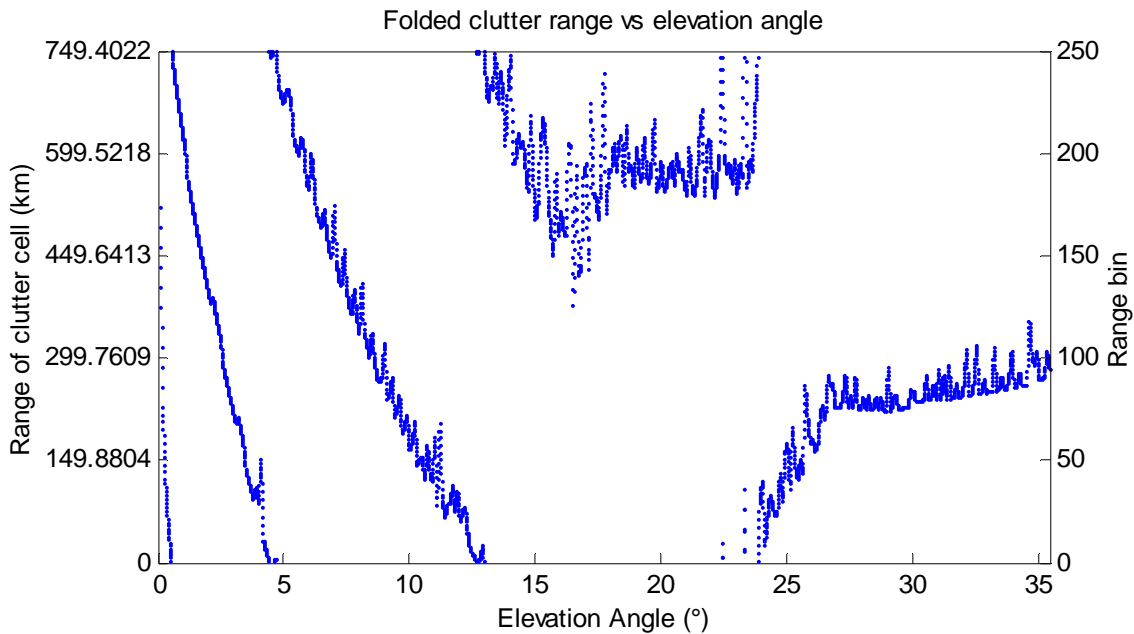


Figure 25. Folded clutter range (path length) vs. elevation angle for  $f_p = 200$  Hz and  $\Delta\theta = 10^{-2}\text{°}$ . Range bins 75 to 90 and 180 to 210 show particularly complex clutter environments.

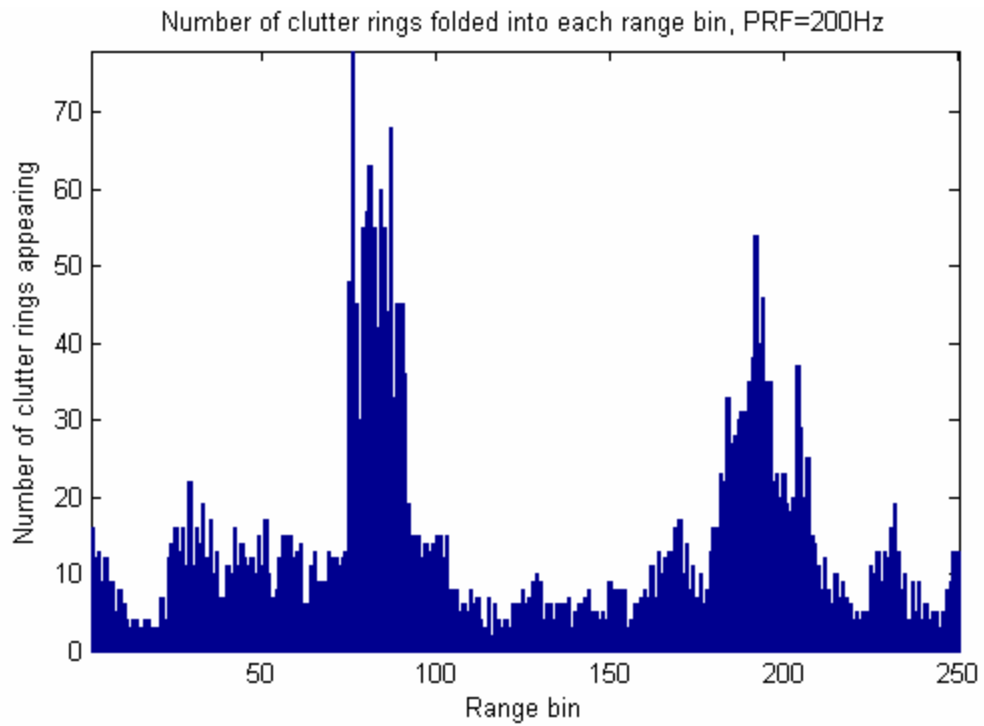


Figure 26. Number of clutter rings in each range bin, for  $f_p = 200$  Hz and  $\Delta\theta = 10^{-2}\text{°}$ .

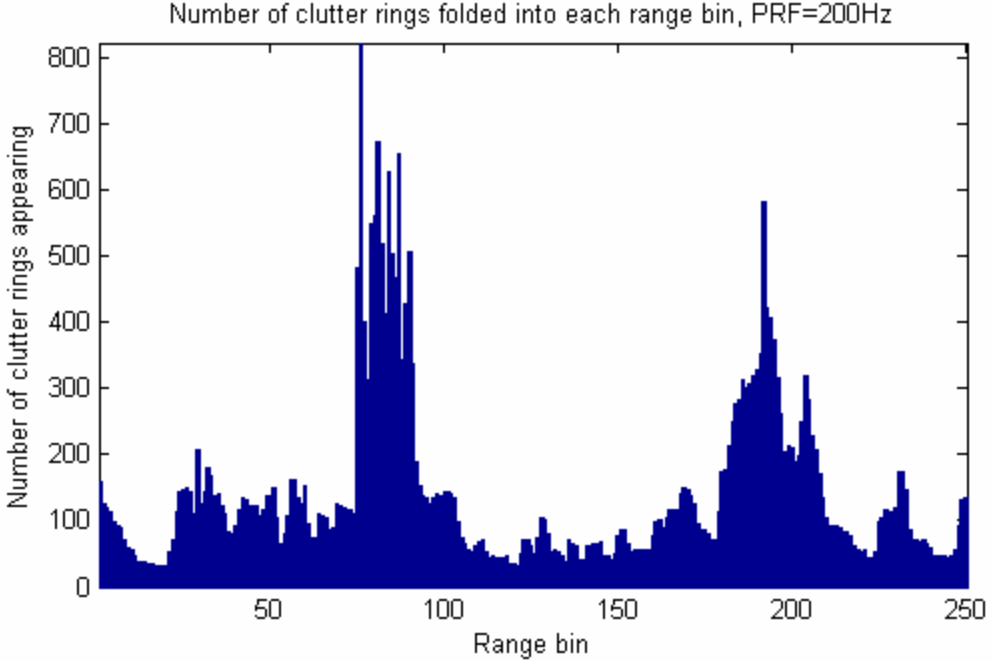


Figure 27. Number of clutter rings in each range bin, for  $f_p = 200$  Hz and  $\Delta\theta = 10^{-3}$ . These numbers do not indicate the true clutter situation, but include artifacts of the interpolation process that are removed in Figure 28.

these duplicate entries are removed from the interpolated paths. Figure 28 shows the numbers of clutter rings with the duplicates removed. Here, the shape is preserved but the peaks are smoothed, greatly reducing the number of rings.

#### 4.5.3 Clutter Return Power

The clutter-to-noise ratio (CNR) for the  $ik^{\text{th}}$  clutter cell from a single radar pulse for each antenna element,  $\xi_{ik}$ , is determined from the radar range equation

$$\xi_{ik} = \frac{P_t G_t(\theta_i, \phi_k) g(\theta_i) \lambda_0^2 \sigma_{ik}}{(4\pi)^3 k T B_n L_s R_i^4}, \quad (27)$$

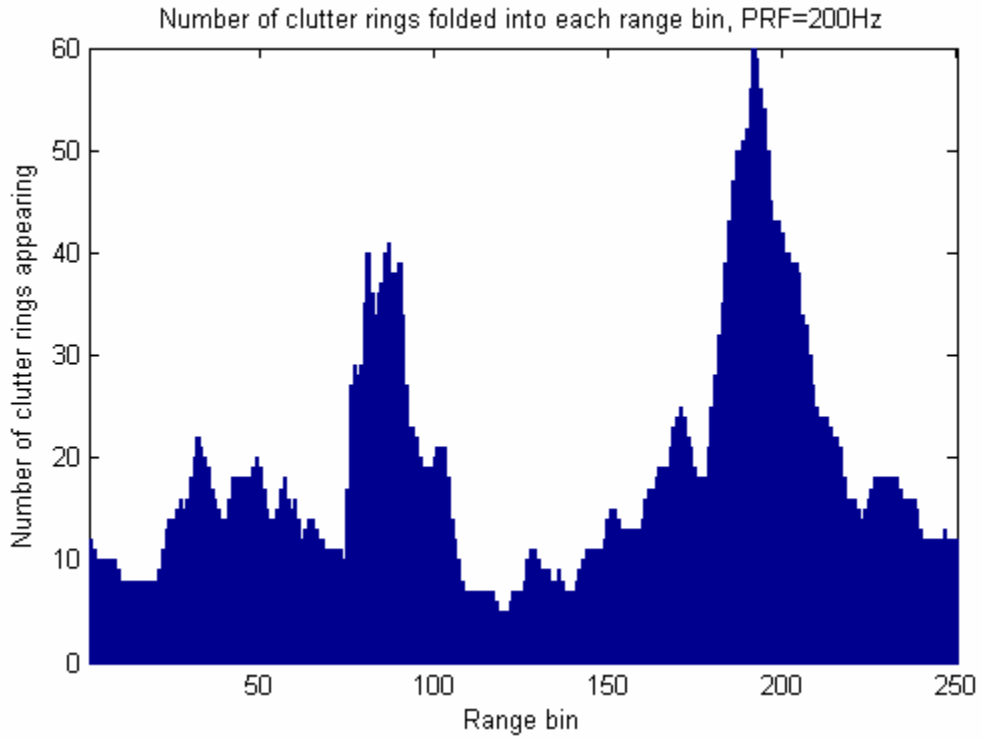


Figure 28. Number of clutter rings in each range bin, with duplicates removed, for  $f_p = 200$  Hz and  $\Delta\theta = 10^{-3}\text{°}$ . The number of clutter cells represents a count across a particular range bin in Figure 25.

where:  $P_t$  is the transmitted power,

$G_i(\theta_i, \phi_k)$  is transmit gain in the direction of the clutter patch,

$g(\theta_i)$  is receive element gain in the direction of the clutter patch,

$\lambda_0$  is signal wavelength,

$\sigma_{ik}$  is clutter patch radar cross-section,

$kTB_n$  is noise power,

$L_s$  is system loss, and

$R_i$  is the refracted path length taken by the signal.

The model in Hale [10], used here, allows the signal return from each radar pulse at each antenna element to be stored and post-processed, with array directionality and pulse integration provided by space and time steering vectors. For this reason,  $\zeta_{ik}$  is the CNR for each antenna element and uses the receive element gain rather than the antenna array gain.

#### 4.5.4 Clutter Covariance

These CNR values are combined into a clutter covariance matrix,  $\mathbf{R}_c$ ,

$$\mathbf{R}_c = \sigma^2 \sum_{i=0}^{N_r-1} \sum_{k=0}^{N_c-1} \xi_{ik} \mathbf{v} \mathbf{v}^H, \quad (28)$$

where  $\sigma^2$  is the thermal noise power,  $N_r$  is the number of clutter rings visible at the target range, and the quantity  $\mathbf{v}(\theta, \bar{\omega}, \phi)$  represents a space-time steering vector defined as

$$\mathbf{v} = \mathbf{e}(\vartheta_z) \otimes \mathbf{b}(\bar{\omega}_{ik}) \otimes \mathbf{a}(\vartheta_x). \quad (29)$$

$\mathbf{v} \mathbf{v}^H$  is equivalent to  $\mathbf{e}(\vartheta_z) \mathbf{e}^H(\vartheta_z) \otimes \mathbf{b}(\bar{\omega}_{ik}) \mathbf{b}^H(\bar{\omega}_{ik}) \otimes \mathbf{a}(\vartheta_x) \mathbf{a}^H(\vartheta_x)$ . The  $\mathbf{x}^H$  notation represents the Hermitian, or conjugate-transpose matrix operation, and  $\otimes$  represents the Kronecker product. The elevation and azimuth components of the steering vector,  $\mathbf{e}(\vartheta_z)$  and  $\mathbf{a}(\vartheta_x)$ , are

$$\mathbf{e}(\vartheta_z) = [1 \quad e^{j2\pi\vartheta_z} \quad \dots \quad e^{j2\pi(P-1)\vartheta_z}], \quad (30)$$

and

$$\mathbf{a}(\vartheta_x) = [1 \quad e^{j2\pi\vartheta_x} \quad \dots \quad e^{j2\pi(N-1)\vartheta_x}],, \quad (31)$$

where  $N$  and  $P$  are the number of elements in the  $N \times P$  antenna array. For the single row of elements in the OTHR antenna,  $P = 1$ , and so  $\mathbf{e}(\vartheta_z) = 1$ . The quantity  $\vartheta_x$  represents the spatial frequency  $x$  component of the antenna, as seen by a point scatterer at  $\theta$  and  $\phi$ , and is found by

$$\vartheta_x = \frac{d_x \cos \theta \sin(\phi + \pi/2)}{\lambda_0}, \quad (32)$$

and  $d_x$  is the distance between antenna elements along the x-axis, for an array oriented along the x-axis. The  $\pi/2$  is included to account for the different definition of  $\phi$  between the Hale/Ward model and this model.

Similarly, the temporal steering vector  $\mathbf{b}(\bar{\omega}_{ik})$  is

$$\mathbf{b}(\bar{\omega}) = [1 \quad e^{j2\pi\bar{\omega}} \quad \dots \quad e^{j2\pi(M-1)\bar{\omega}}] \quad (33)$$

where  $M$  is the number of pulses integrated and  $\bar{\omega}$  is the normalized Doppler frequency of the clutter patch found from

$$\bar{\omega} = \frac{2v_c \cos \theta \sin \phi}{\lambda_0 f_p}. \quad (34)$$

The term  $v_c \cos \theta \sin \phi$  is the relative velocity of the clutter patch with velocity  $v_c$  and  $f_p$  is the radar pulse repetition frequency (PRF).

In general, the clutter patches are not moving and have zero velocity. However, the moving ionosphere introduces a Doppler spreading, which can be represented by clutter motion. The system is first examined without this Doppler spreading, leaving  $\mathbf{b}(\bar{\omega}_{ik}) = 1$ . Later, internal clutter motion (ICM) is introduced through temporal decorrelation of the clutter covariance matrix [12:58-59], and accounts for ionospheric motion.

This decorrelation changes the  $\mathbf{b}\mathbf{b}^H$  term in (28), so that

$$\mathbf{b}(\bar{\omega}_{ik})\mathbf{b}^H(\bar{\omega}_{ik}) = \rho_{mp}^{(C)} \exp(j2\pi\bar{\omega}_{ik}m - j2\pi\bar{\omega}_{ik}p). \quad (35)$$

Here,  $m$  and  $p$  denote successive pulses, and  $\rho_{mp}^{(C)}$  is

$$\rho_{mp}^{(C)} = e^{-\frac{B_c^2}{8}(m-p)^2}, \quad (36)$$

where  $B_c$  is the clutter bandwidth, normalized by the radar bandwidth.

As for the noise covariance of (23), the clutter covariance matrix is equivalent to the expected value of the product of a clutter snapshot  $\chi_c$  with its conjugate-transpose, or

$$\mathbf{R}_c = \mathbb{E}\{\chi_c \chi_c^H\}. \quad (37)$$

#### 4.6 Atmospheric Noise and Interference

A complete treatment of the OTHR environment would include a model of atmospheric noise and interference, including the interference from other transmitters operating in the same spectral region. This interference tends to be concentrated at specific frequencies in specific directions. It is possible to select the operating frequency so that this interference is minimized, and is at a much lower level than clutter returns [13:120-125]. Hence, this model ignores the atmospheric noise and other incidental interference.

#### 4.7 Total Interference

For processing, the covariance matrices of (23) and (37) are added to form a total interference covariance,  $\mathbf{R} = \mathbf{R}_c + \mathbf{R}_n$ . These are then decomposed to a matrix  $\mathbf{Q}$  using a Cholensky decomposition,  $\mathbf{R} = \mathbf{Q}^H \mathbf{Q}$ .

To get a realization of the radar returns, a random vector  $\mathbf{y}$  of length  $MNP$  is generated and colored by the covariance decomposition:

$$\boldsymbol{\chi}_{H_0} = \mathbf{Q}^H \mathbf{y}. \quad (38)$$

The realization  $\boldsymbol{\chi}_{H_0}$  is now a *time-space snapshot* for the  $H_0$  hypothesis, where no target is present.  $\boldsymbol{\chi}$  has length  $MNP$ , so that  $\boldsymbol{\chi}[1]$  is the voltage return at the first element from the first pulse,  $\boldsymbol{\chi}[2]$  is the return at the second element from the first pulse,  $\boldsymbol{\chi}[N+1]$  is the return at the first element from the second pulse, up to  $\boldsymbol{\chi}[MNP]$ , the return at the last element for the last pulse. The interference power  $P_n$  of a specific realization is then

$P_n = \left| \mathbf{v}_t^H \boldsymbol{\chi}_{H_0} \right|^2$ , where  $\mathbf{v}_t$  is a steering vector in the target direction and at the target's normalized Doppler frequency.

#### 4.7.1 Statistical Realization

Radar performance analysis requires analyzing a number of trials of each case, to determine detection and false alarm probabilities,  $P_d$  and  $P_{fa}$ . A specified false alarm probability requires  $10/P_{fa}$  trials of the  $H_0$  hypothesis (no target present) for this Monte Carlo analysis. The detection threshold is then set at a level giving 10 false alarms from the set of trials.

For target detection, a target return is added to the original  $\boldsymbol{\chi}_{H_0}$  snapshot to give  $\boldsymbol{\chi}_{H_1}$ , a snapshot with a target present

$$\boldsymbol{\chi}_{H_1} = \boldsymbol{\chi}_{H_0} + \mathbf{v}_t \sqrt{SINR \cdot \mathbf{R}(1,1)}. \quad (39)$$

In this expression,  $\mathbf{v}_t$  represents the phase differences of the returns from element-to-element and pulse-to-pulse, from a scatterer in the target direction and at the target's Doppler frequency.  $\mathbf{R}(1,1)$  is the average interference power and  $SINR$  is the target signal-to-interference-plus-noise ratio.  $\mathbf{R}$  and  $SINR$  are power terms, so the square root is taken to convert to a voltage. The received power with a target present,  $P_{sn}$ , is then

$$P_{sn} = \left| \mathbf{v}_t^H \boldsymbol{\chi}_{H_1} \right|^2.$$

This process is repeated for a range of target SINR values. If  $P_{sn}$  is greater than the threshold, then the target is detected. The ratio of detections to the total number of trials gives a detection probability for that SINR. For a specified  $P_d$  requirement, the minimum SINR at which this  $P_d$  is achieved defines the minimum target RCS.

This minimum target RCS comes from a modified form of the range equation. The standard equation in [21:34] is rearranged to solve for target RCS. Because of the presence of clutter, the noise power  $kTB_n$  is replaced by the average interference power  $\mathbf{R}(1,1)$ , and the minimum target RCS is

$$\sigma_{t_{\min}} = \frac{SINR_{\min} (4\pi)^3 R_t^4 \mathbf{R}(1,1) L_s}{P_t G(\theta, \phi) g(\theta) \lambda_0^2}. \quad (40)$$

Initial model confirmation comes from Albersheim's equation [21:43-45]. Restricting the receiver processing to a single element and single pulse allows standardization between different radar configurations and gives the plot shown in Figure 29, for  $P_{fa} = 10^{-3}$ . This plot matches the plot shown in Skolnik [21:44].

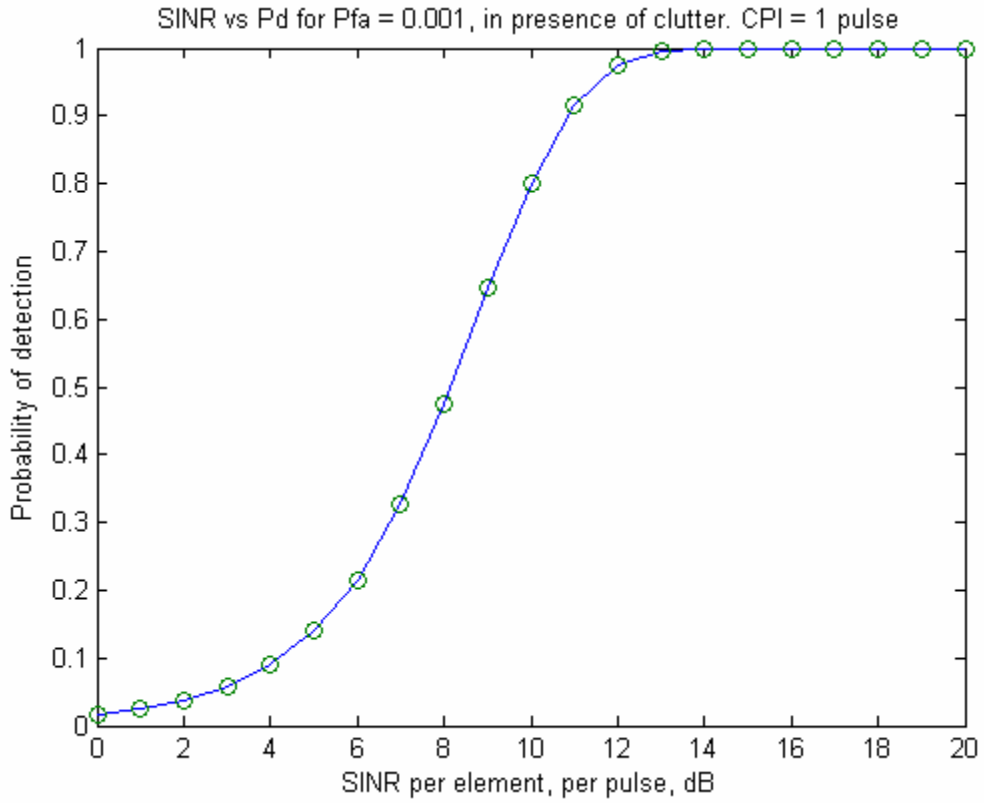


Figure 29. SINR per element, per pulse, for  $P_{fa}=10^{-3}$ . Restricting radar processing to a single pulse and a single element allows standardization between radars.

#### 4.8 Clutter Structure

The clutter return power has an azimuth dependence that follows the antenna element pattern and is centered on zero hertz, as it is stationary. The clutter return spread corresponds to the Doppler filter bandwidth, introduced by integrating pulses.

Two approaches are required to describe the true clutter structure: a minimum variance method gives better resolution but loses amplitude information, and a Fourier method gives amplitude information but provides poorer resolution. For target detection, the radar returns are processed using a Fourier-based method, so the Fourier PSD more closely reflects the clutter's impact on radar detection performance.

The minimum variance representation of the clutter power spectral density (PSD) for  $f_p = 200$  Hz and 10 coherent pulses is shown in Figure 30, where dark areas correspond to higher power density. A clutter PSD plot customarily shows range and Doppler dependence. In this model, the clutter range is dependent on the signal elevation on transmission, because of the ionospheric refraction. Because the antenna is not steerable in elevation, the figure shows an azimuth-Doppler plot. This minimum variance PSD is found from [12:102]:

$$PSD_{mv} = (\mathbf{v}^H \mathbf{R}^{-1} \mathbf{v})^{-1}, \quad (41)$$

where  $\mathbf{v}$  is the steering vector in azimuth, elevation and Doppler, and  $\mathbf{R}$  is the total interference covariance matrix. The clutter is centered on zero Hertz, as expected for a stationary platform. The slight spreading is because of the response of the minimum variance function.

Similarly, the Fourier PSD is found from [12:100]:

$$PSD_F = \mathbf{v}^H \mathbf{R} \mathbf{v}. \quad (42)$$

The Fourier clutter PSD response is shown in Figure 31, for  $M = 10$  pulses and  $f_p = 200$  Hz. In azimuth, the response follows the antenna pattern, and has a Doppler pattern corresponding to the Fourier transform of the number of pulses integrated, giving  $M-1$  nulls in Doppler response between main clutter peaks. The clutter levels outside of

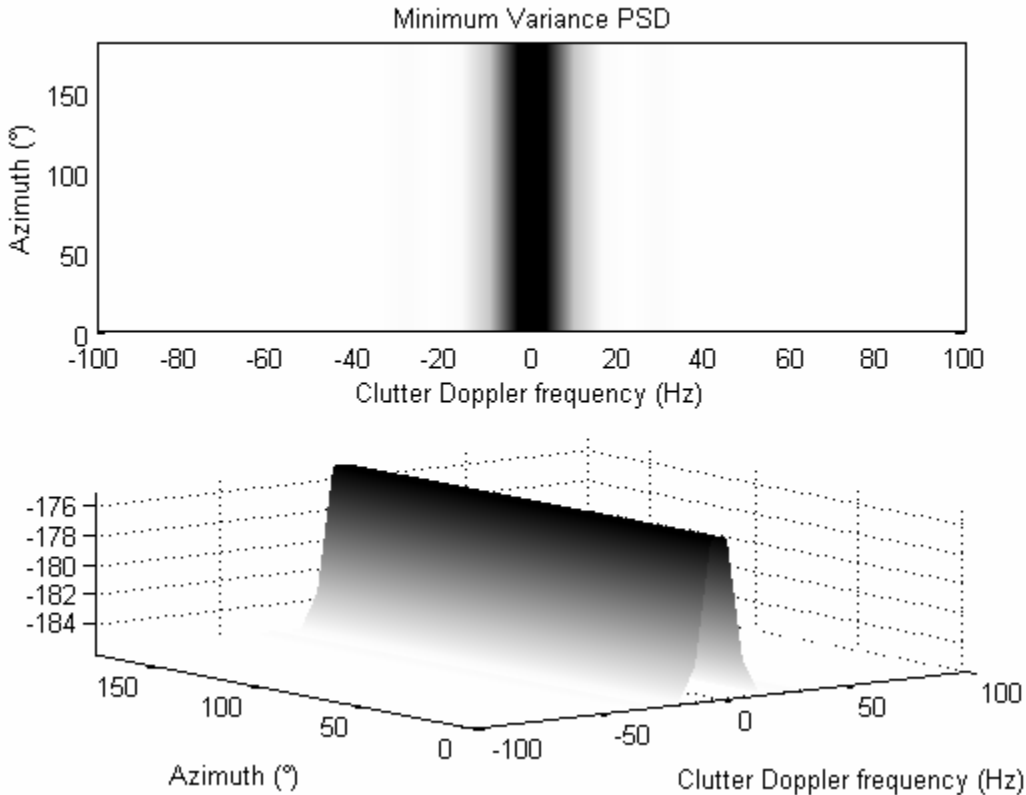


Figure 30. Minimum Variance Power Spectral Density of clutter, for  $f_p = 200$  Hz and  $M = 10$ . Dark areas correspond to higher power density.

these nulls are very high. Chapter 5 examines the target sizes necessary for detection in this clutter.

Integrating more pulses reduces the levels of clutter due to the better Doppler filter properties resulting from increasing  $M$ . Figure 32 shows the minimum variance PSD while Figure 33 shows the Fourier PSD for  $M = 30$  pulses and  $f_p = 200$  Hz. Here, the Doppler spread of the clutter is reduced as are the clutter levels away from the 0 Hz peak. Target detection in clutter is dependent on the number of pulses integrated, as will be shown in Chapter 5.

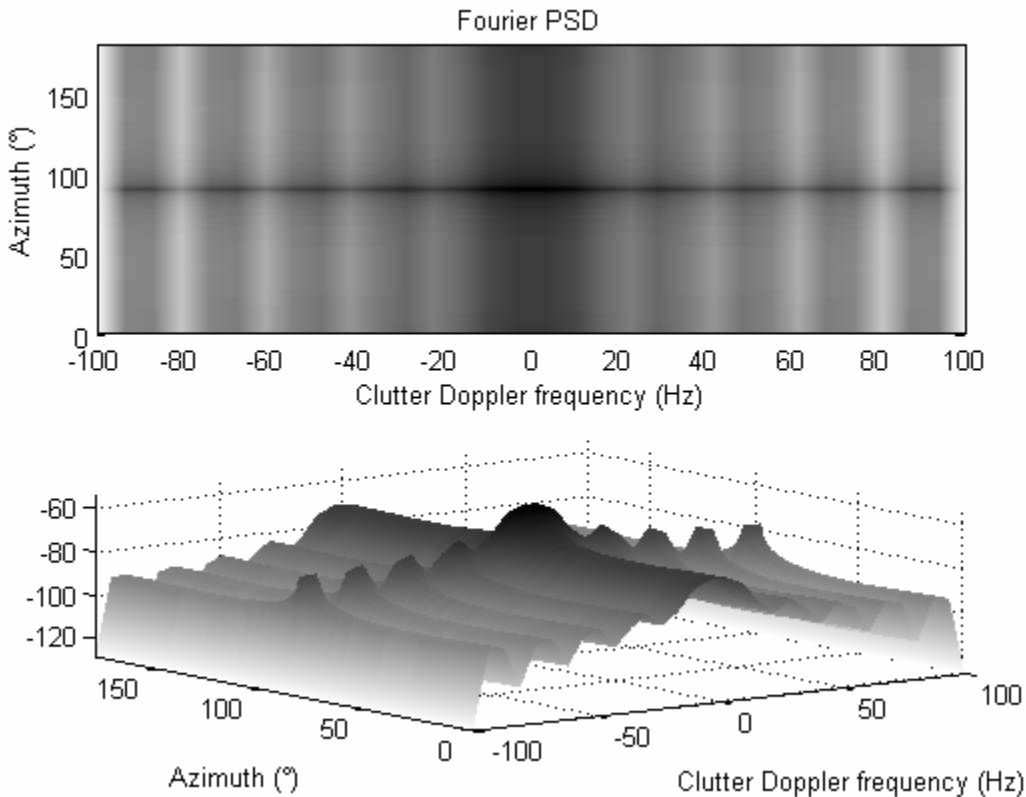


Figure 31. Fourier Power Spectral Density of clutter, for  $f_p = 200$  Hz and  $M = 10$ .

#### 4.9 Summary

The radar clutter environment combines the antenna array and ionospheric models and allows determination of the minimum detectable target size for a certain position and velocity.

There are a large number of variables greatly affecting system performance. This chapter presented a limited set of values to characterize the models used. Chapter 5 further explores the effect of changing the model parameters on the system performance.

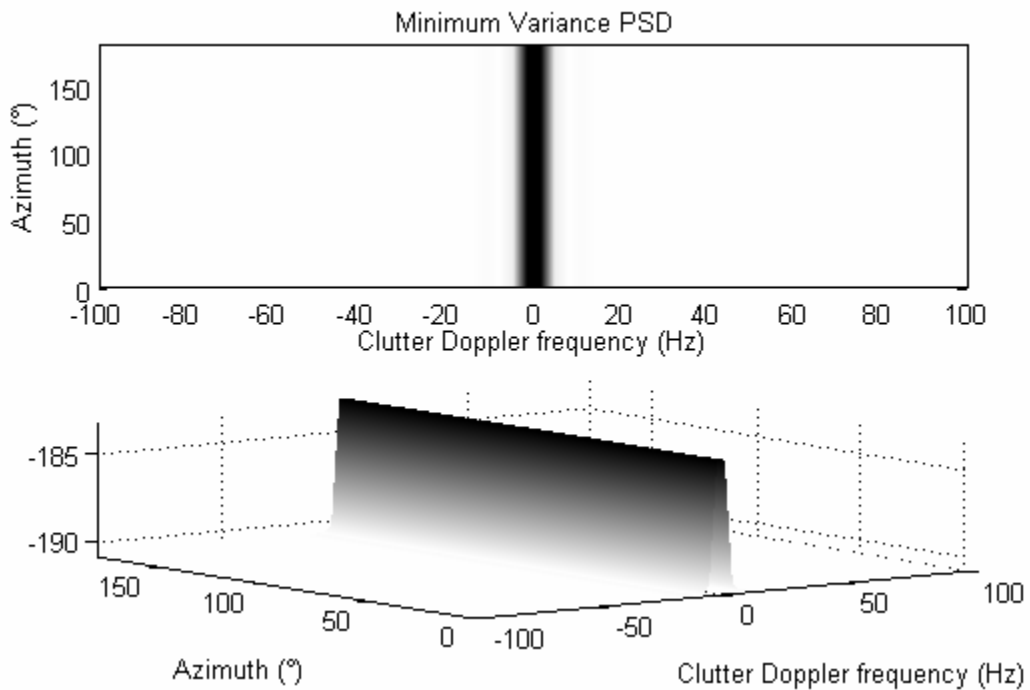


Figure 32. Minimum variance Power Spectral Density of clutter, for  $f_p = 200$  Hz and  $M = 30$ . The true clutter power is narrowly distributed around 0 Hz.

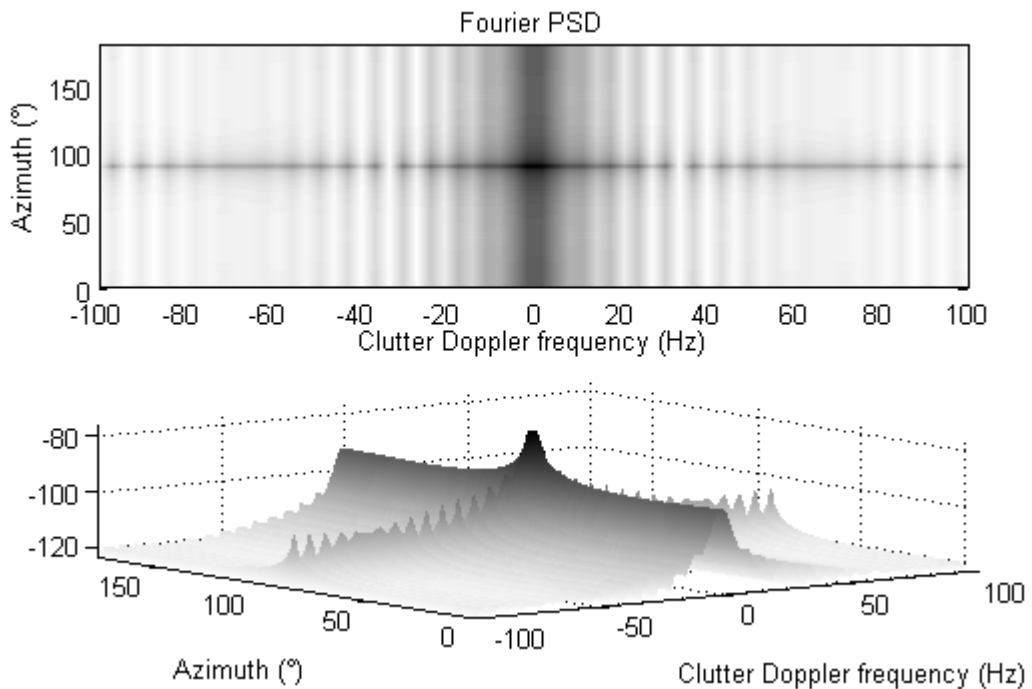


Figure 33. Fourier Power Spectral Density of clutter, for  $f_p = 200$  Hz and  $M = 30$ . The Doppler side lobes are reduced, but are still apparent

## V. Analysis of Results

### 5.1 Chapter Overview

The previous chapters characterized the radar operating environment, and now allow analysis of the radar's performance potential. This chapter describes the modeling results and then relates these results to matching operational scenarios. The radar operating parameters are varied to simulate different target positions and velocities, with results indicating limits on detectable target sizes. Several techniques to improve radar performance are discussed.

### 5.2 General Considerations

The analysis is limited to low-earth-orbit (LEO) targets with orbital altitudes of 200 to 2000 km. Setting the target position at the center of the elevation sidelobe provides the best possible performance and is used for all test cases. As shown in Figure 20, very little power penetrates the ionosphere outside of this sidelobe.

Because the maximum height at which the ionosphere returns a ray path to earth is approximately 300 km, a small subset of possible target trajectories lies in the upper edge of the main antenna beam. The power levels in this region are similar to those in the elevation sidelobe, so these target trajectories are not considered separately.

### 5.3 Noise Limited Case

Although clutter can never be completely negated, analysis of the radar model without clutter provides a baseline for model performance that can never be bettered. In the noise limited case, the minimum RCS for a detectable target is determined by (40).

The key parameter is the minimum target SINR, which in turn depends on the specified false alarm and detection probabilities,  $P_{fa}$  and  $P_d$ . The minimum RCS for the noise limited case is shown in Figure 34, for  $P_{fa} = 0.01$  and  $P_d = 0.95$ . To confirm against (40), the following parameters are applied:

$$\begin{aligned} SNR_{\min} &\approx 10 \text{ dB} - AF_{peak} = 10 - 19 \text{ dB} \equiv 10/82 \text{ (unitless)} \\ R_t &= 500 \text{ km} \\ \mathbf{R}(1,1) &= kTB_n = 1.381 \times 10^{-23} \times 300 \times 50000 = 2.071 \times 10^{-16} \text{ W} \\ L_s &= 2 \text{ (unitless)} \\ P_t &= 12 \text{ MW} \\ G_t(\theta_i, \phi_k) &= 55.61 \text{ (unitless)} \\ g(\theta_i) &= 0.678 \text{ (unitless)} \\ \lambda_0 &= 9.993 \text{ m} \end{aligned}$$

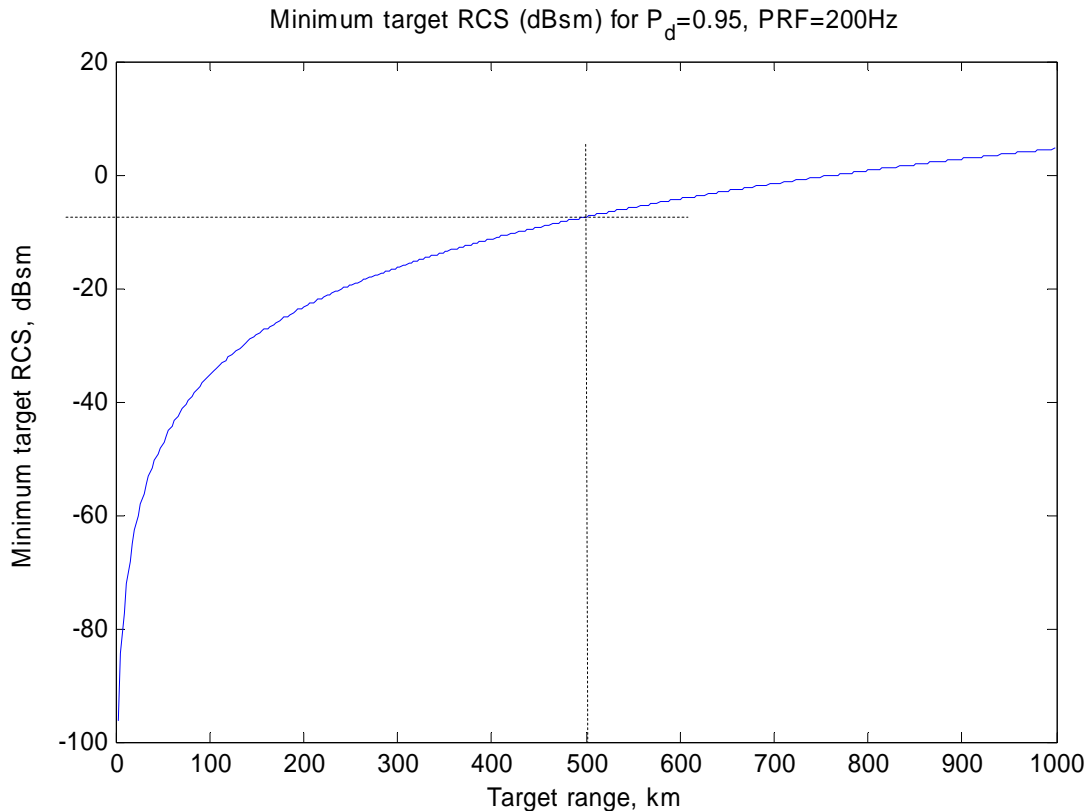


Figure 34. Minimum Target RCS vs. Range, noise only, for  $P_{fa} = 0.01$  and  $P_d = 0.95$ .

The minimum SNR comes from the plots of Albersheim's equation in Skolnik [21:44], for  $P_{fa} = 0.01$  and  $P_d = 0.95$ . These plots are for a single element, whereas the calculated RCS shown in Figure 34 is for the entire array and includes the array factor peak gain of 82 (19 dB). As a result, the actual SNR requirement is divided by this peak gain to give the equivalent single element SNR. The minimum target RCS at a range of 500 km is then

$$\sigma_{t_{\min}} = \frac{SINR_{\min} (4\pi)^3 R_t^4 \mathbf{R}(1,1) L_s}{P_t G(\theta, \phi) g(\theta) \lambda_0^2} = 0.139 \text{m}^2 = -8.58 \text{dBsm}. \quad (43)$$

The minimum target RCS shown on Figure 34, for the same range, is -7.44 dBsm. This figure is calculated using results from a  $P_d$  analysis with SNR steps of 2 dB, so the SNR used to generate the plot is -8 dB, compared to -9.14 dB in the manual calculation. This difference of 1.14 dB is exactly the difference in the RCS values, as should occur, and so validates the model for the noise-limited case. In other words, the results exactly match those predicted by Albersheim's equation at  $R_t = 500$  km.

#### 5.4 Introduction of Clutter

The clutter power seen by the system is far greater than the noise power. Because of aliasing in range, the clutter power in a given range bin is dependent on the pulse repetition frequency,  $f_p$ . Figure 35 shows the clutter power for  $f_p = 200$  Hz over the unambiguous range of the radar.

The shape of Figure 35 bears a resemblance to that of Figure 28; the differences are caused by the different antenna gains at the different elevation angles. Some clutter rings are seen at or near peak power, while others are at or near nulls.

## 5.5 Target Detection in Clutter

When clutter is introduced into the RCS calculations, the required RCS increases considerably. Using a single pulse gives the results shown in Figure 36. The minimum required RCS is far greater than that of any realistic target, except for very short ranges that are below the minimum target altitude, meaning that Doppler processing is required to detect targets. Doppler processing equates to integrating multiple pulses.

With target positions constrained to lie near the elevation sidelobe center, the target Doppler frequency  $f_d$  will have a maximum of 1230 Hz for a target traveling at 7.8 km/s on an overhead trajectory. Targets not passing overhead have lower Doppler frequencies, limited to 0 Hz for a target traveling tangentially.

Repeating the calculations for selected ranges and 10 integrated pulses gives the results shown in Figure 37 for  $f_p = 200$  Hz and target Doppler frequency  $f_d = 850$  Hz. The figure shows large values of required target RCS; this Doppler frequency corresponds to a sidelobe in the Doppler response of the clutter. The calculation for 10 pulses is computationally intensive and the large step size between ranges is introduced to allow realistic calculation times.

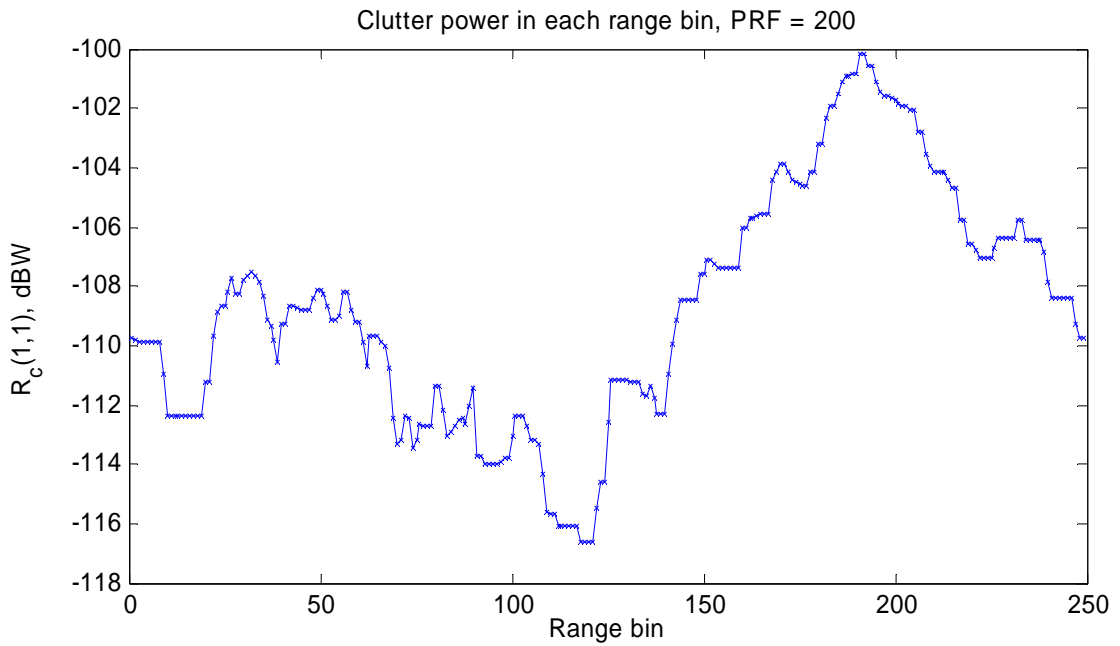


Figure 35. Clutter power seen at each range bin, for  $f_p = 200$  Hz.

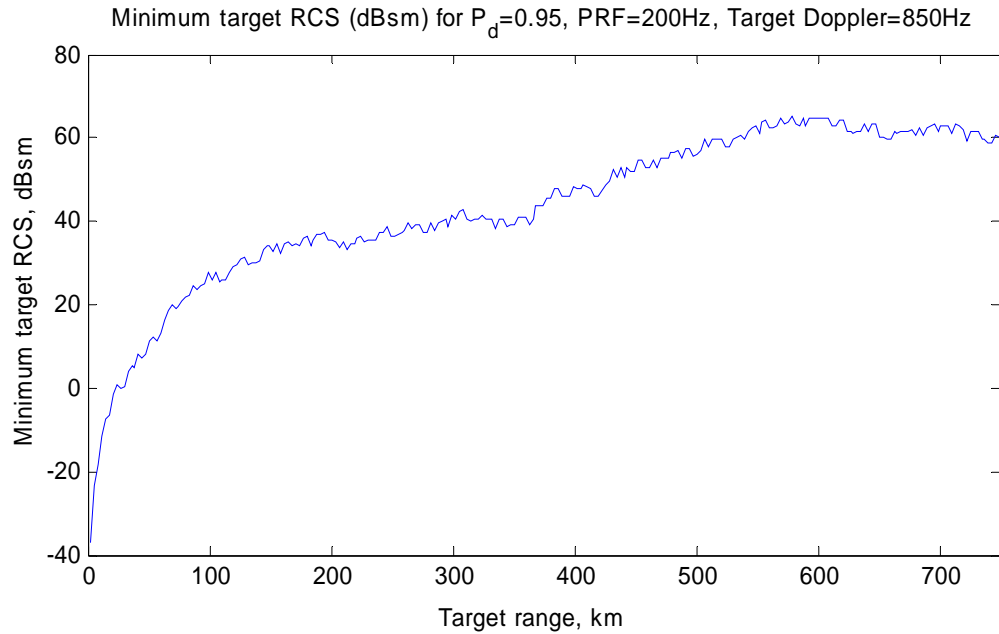


Figure 36. Minimum target radar cross-section vs. range for  $f_p = 200$  Hz, no pulse integration, over the radar's unambiguous range.

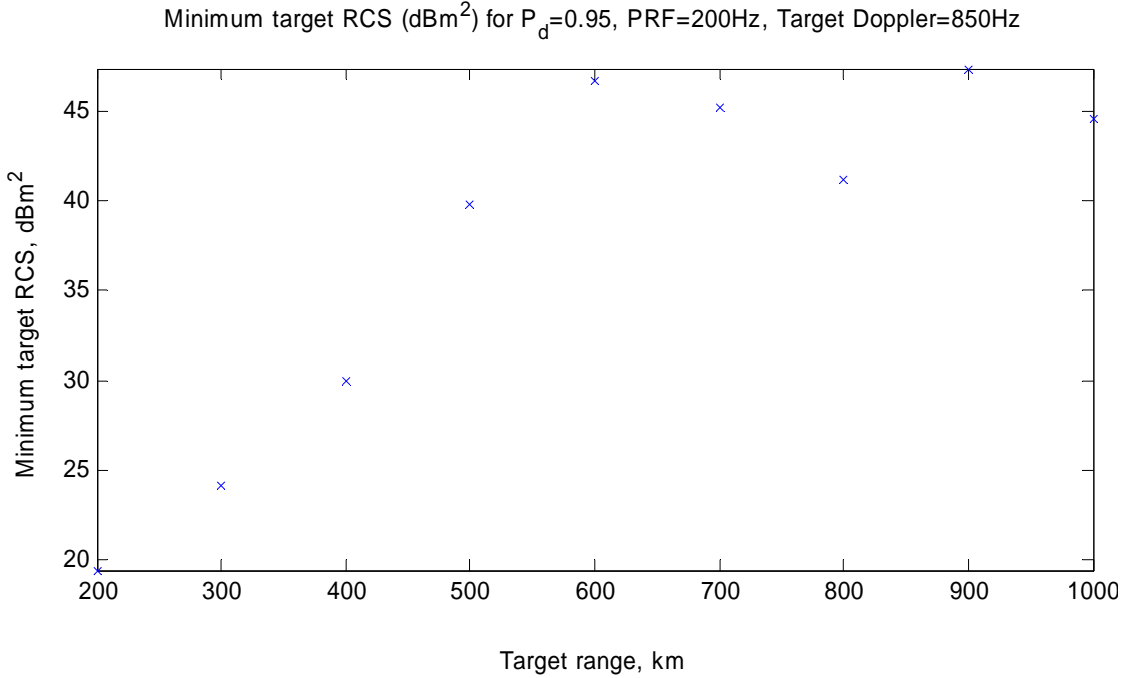


Figure 37. Minimum radar cross-section for  $M = 10$ , with  $f_p = 200$  Hz and  $f_d = 850$  Hz, for a representative set of target ranges. Ranges from 750-1000 km are ambiguous and are folded into the clutter from ranges 0-250 km.

Plotting the required RCS against target Doppler frequency shows the strong dependence on target velocity. Figure 38 shows the minimum required target RCS for  $M = 10$  integrated pulses. Away from the nulls, the detectable sizes are still large compared to most space targets. The large peak at 800 Hz corresponds to the 0 Hz main clutter lobe, aliased to a multiple of  $f_p$ . The Fourier detection method causes the Doppler side lobes.

However, for the 20 integrated pulses shown in Figure 39, the minimum required target RCS approaches reasonable target sizes, away from the main clutter lobe. The patterns in these minimum RCS plots correspond to the Doppler pattern of the clutter

Fourier PSD, from Figure 31 and Figure 33. Integrating more pulses gives narrower Doppler filtering, providing more isolation from the 0 Hz clutter peak.

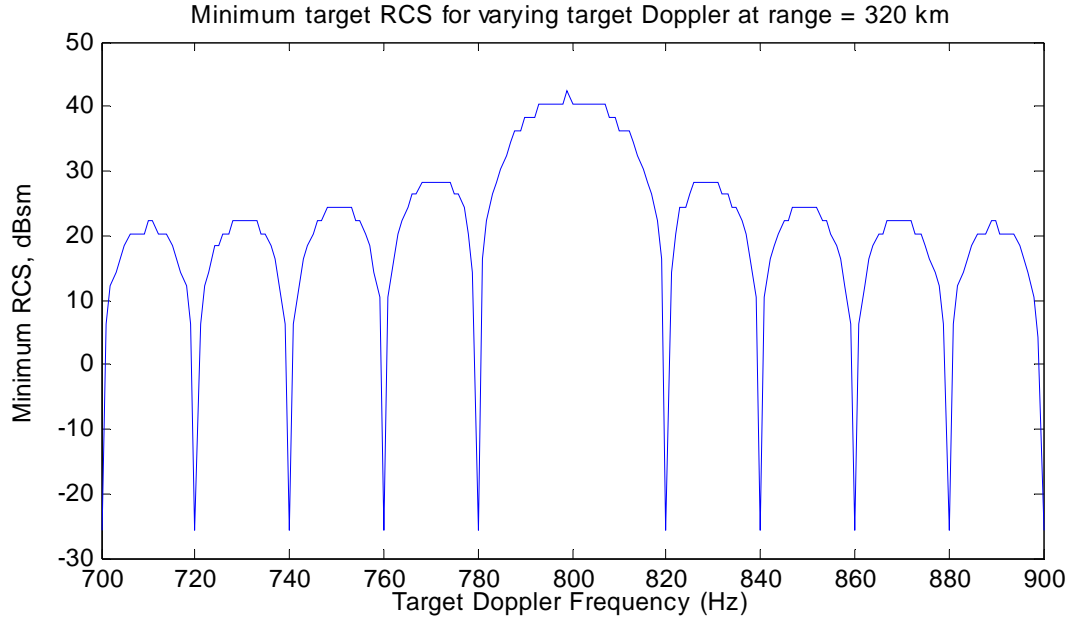


Figure 38. Minimum radar cross-section vs. Doppler frequency for  $f_p = 200$  Hz and  $M = 10$  pulses, target range = 320 km.

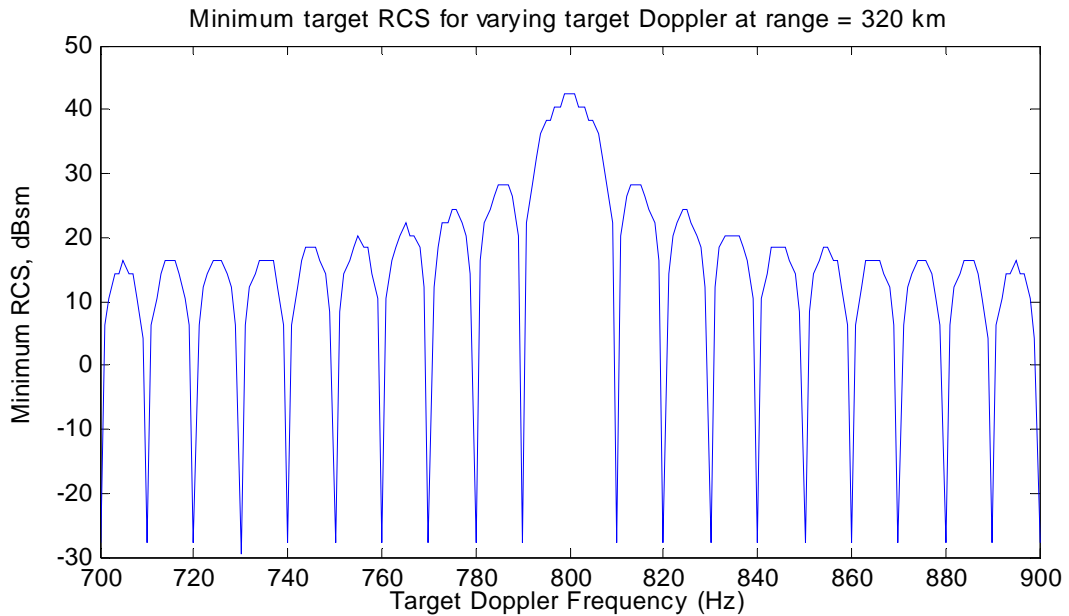


Figure 39. Minimum radar cross-section vs. Doppler frequency for  $f_p = 200$  Hz and  $M = 20$  pulses, target range = 320 km.

## **5.6    Limits on Coherent Pulse Integration**

The high velocities of potential targets (up to 7.8 km/s), together with the low pulse repetition frequency required to give a workable unambiguous range, mean that the number of pulses available for coherent integration is limited. For a target traveling at 7 km/s with  $f_p = 100$  Hz, integrating even 20 pulses can give a relative motion of more than 1 km. If the target's trajectory is not directly radial, this motion moves the target over the antenna's narrow azimuth pattern. The changing power level lessens pulse coherence and reduces the radar's ability to detect the target.

## **5.7    Limits on Doppler Space**

The available Doppler space is analogous to the unambiguous range, and is limited to the pulse repetition frequency. Target Doppler frequencies of  $f_d + n f_p$  are aliased to  $f_d$  and so are indistinguishable. A higher pulse repetition frequency gives a greater Doppler space at the expense of decreasing unambiguous range, aliasing more clutter range rings into the target range bin. With target Doppler frequencies expected up to approximately 1200 Hz, an  $f_p$  of 1200 Hz would be needed to provide adequate Doppler space. This PRF gives a 125 km unambiguous range, causing large clutter fold-over and effectively removing the radar's ability to determine target range. Lower pulse repetition frequencies will mean that Doppler frequencies for fast-moving targets are aliased, and so it becomes impossible to differentiate space targets from other targets such as aircraft or determine the true velocity of a space-base target, which is important for orbit determination.

The OTH-B system specifications [17] give the PRF range as 10 to 60 Hz; however this is an FM-CW specification and is designed for standard OTHR operations. The remainder of this model will ignore this restriction.

## 5.8 Interpulse Modulation

The main method used to mitigate this range-Doppler space tradeoff is interpulse (pulse-to-pulse) modulation. Successive pulses are modulated, or ‘chirped’, in different patterns, so that one pulse has orthogonality from the next, and can be separated by the receiver. Chirp codes can cover two or more pulses; however, there are practical limits to the degree of orthogonality achieved which limits the length of chirp codes [10:44-70]. While the actual methods for interpulse modulation in the transmitter and receiver are not included in this model, the effects can be simulated, for small numbers of pulses, by simply redefining and extending the unambiguous range,  $R_u$ , as

$$R_u = \frac{nc}{2f_p}, \quad (44)$$

where  $n$  is the number of uniquely coded pulses.

Interpulse modulation also increases range resolution by effectively decreasing pulse width and range bin size [10:18-21,35]. Clutter ring width is decreased and so is the interference power from the ring. This analysis ignores the *pulse compression* to show how eliminating clutter fold-over greatly improves system performance

For a PRF of 1200 Hz, a 16 pulse code gives  $R_u = 2000$  km, the same as a direct 75 Hz PRF and sufficient to cover the range space analyzed in this model. This PRF also allows a greater number of pulses to be integrated without losing coherence. Using these

parameters removes most clutter range and Doppler aliasing and improves detectable target size, as shown in Figure 40 for  $M = 10$  pulses.

This RCS range now encompasses most space targets of interest. The stepped shape of this graph occurs because the model is calculated in steps of 2 dB for  $SINR$ , and so gives 2 dB steps for minimum RCS. These parameters also change the observed clutter PSD. The Fourier PSD is shown in Figure 41.

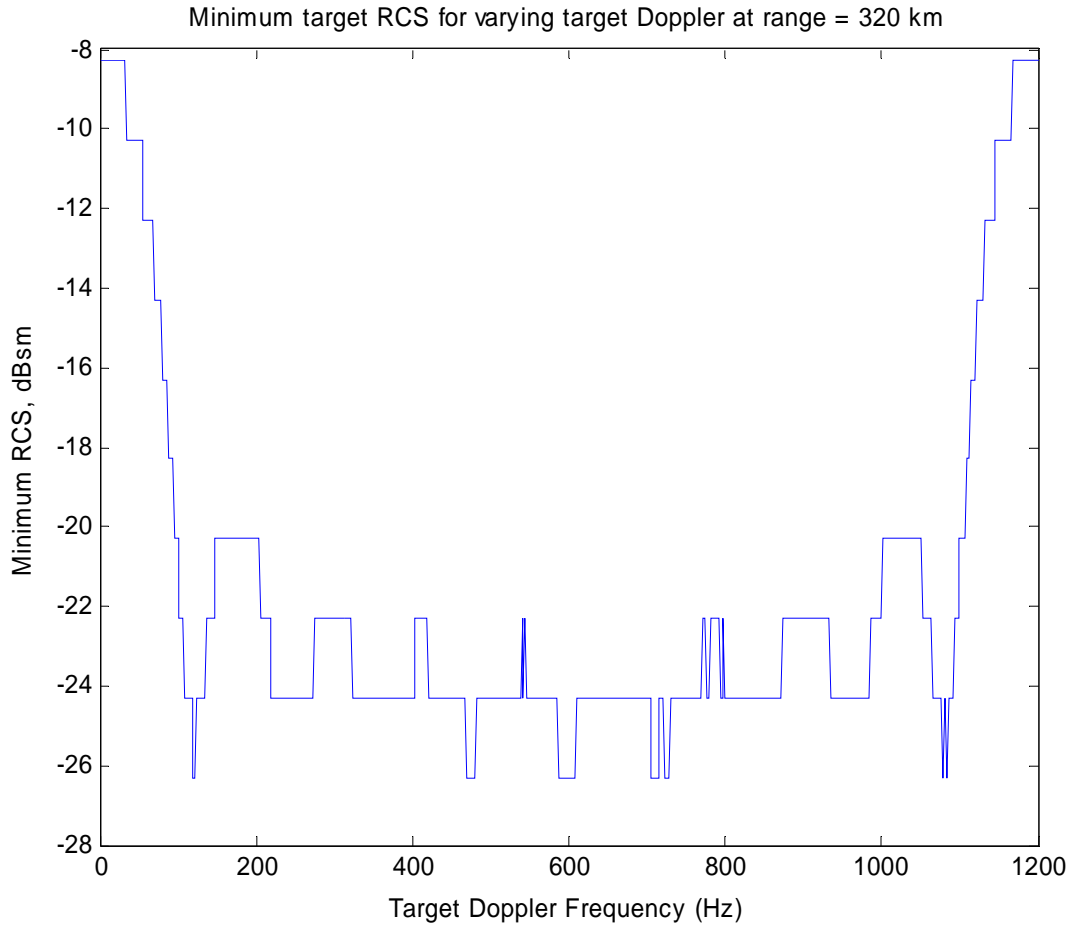


Figure 40. Minimum target RCS for  $f_p = 1200$ ,  $M = 10$ , 16 interpulse codes, with target range = 320 km.

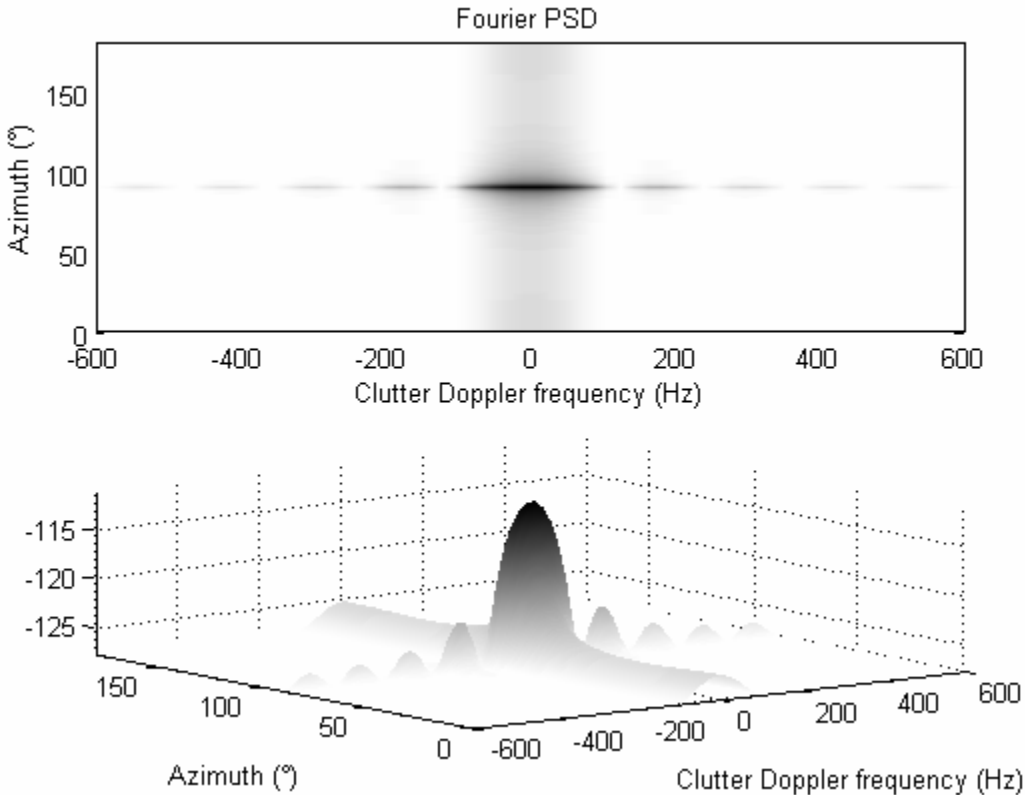


Figure 41. Fourier PSD for  $f_p = 1200$ ,  $M = 10$ , 16 interpulse codes, with range = 320 km. The Doppler side lobes are now greatly reduced.

## 5.9 Internal Clutter Motion

To simulate the effect of ionospheric motion on the clutter return, an internal clutter motion (ICM) term is included in the clutter covariance matrix. With a 3 Hz clutter bandwidth, the clutter power spreads into the narrow nulls visible in Figure 38 and Figure 39. As more pulses are integrated and the unambiguous range and Doppler space increase, the nulls are less pronounced and ICM has less effect. Figure 42 is the equivalent of Figure 40 with ICM included. This set of PRF and interpulse coding

parameters ensures that the small amount of Doppler spreading introduced by ICM has little effect.

### 5.10 Summary

While detection of space targets is possible with the system as modeled, there are several operational constraints that will make the conditions required for detection less achievable. Firstly, OTHR systems normally operate at frequencies designed to illuminate patches of ground. Such frequencies are lower than the system maximum analyzed here. As is evident in Figure 5, operating at lower frequencies means the

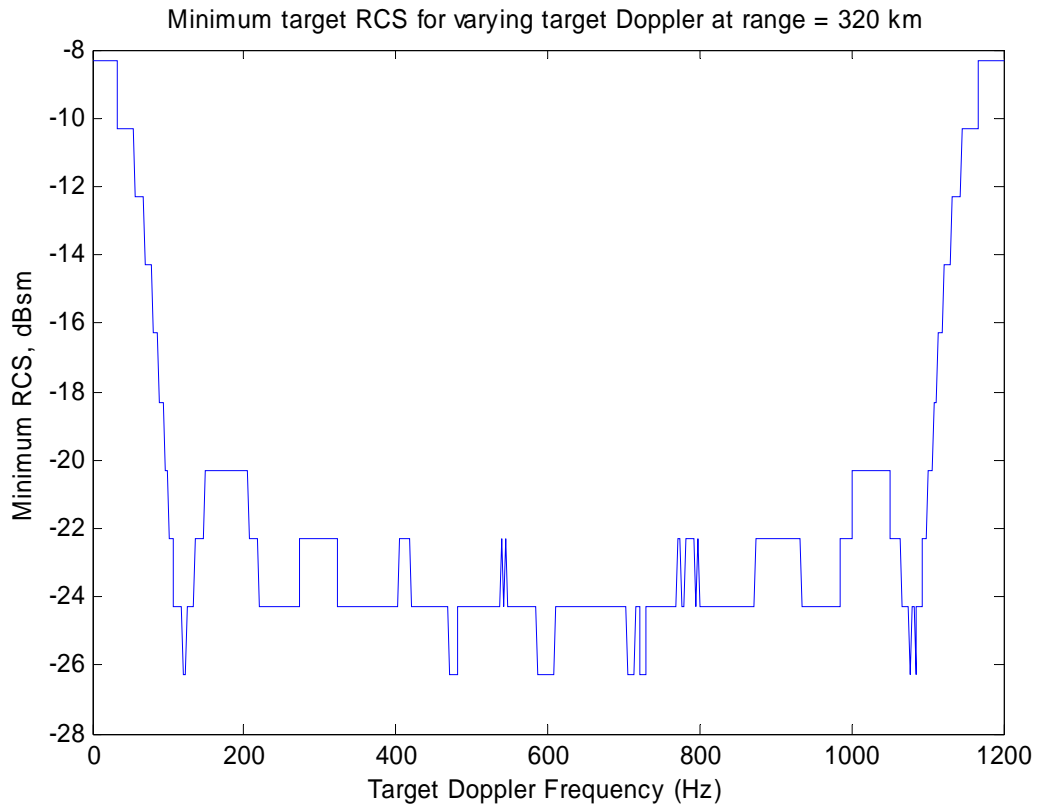


Figure 42. Minimum RCS for  $f_p = 1200$ ,  $M = 10$ , 16 pulse coding, with range = 320 km, with ICM included.

cutoff angle for radiation to penetrate the ionosphere is higher, and often higher than the upper edge of the elevation sidelobe shown in Figure 12. This result means power levels reaching a target are reduced by 20 dB or more, with a commensurate rise in required RCS for detection. Further, as the elevation angle to the target increases, the target Doppler frequency decreases, so that the target return approaches the clutter in Doppler space. This result implies that the coverage region for detection is further reduced from the already narrow region.

Another factor is that the wide elevation beamwidth means the system has no ability to determine the elevation angle to the target, except by inference from observed range and Doppler frequency and assuming certain orbital characteristics. This limitation reduces the system's utility for orbit determination.

The other motivation for space surveillance is missile warning. In its launch phase, a missile is in the realm of an OTHR in its traditional role. In the boost phase, the missile is likely to be outside the radar's range, often being at several thousand kilometers altitude. In the terminal phase, the warhead has separated from its earlier stages and is a small target, electrically and physically, similar in size and properties to a satellite. It may be in range of the OTHR in "space surveillance mode"; however, by the time the warhead gets within the radar's coverage zone, it is only seconds away from impact. Hence, the OTHR does not provide great utility for missile detection above the ionosphere

## **VI. Conclusions and Recommendations**

### **6.1 Overview**

This chapter presents a summary of conclusions reached in the course of preparing this thesis, as well as appropriate recommendations on further work that may follow.

The models presented here for the ionosphere, antenna array, clutter environment and radar processor allow simulation of OTHR performance in a space surveillance role. The antenna array model describes the power distribution from the radar transmitter, based on published parameters for the AN/FPS-118 OTH-B. The ionospheric model allows calculation of path propagation, given an elevation angle from the antenna array. Together, these models describe the power distribution and spreading in the system.

The clutter environment and radar model define how clutter is seen by the radar. The clutter power is dependent on target range and on radar operating parameters including the pulse repetition frequency (PRF).

Target detection is also very dependent on the PRF, with higher target velocities requiring a higher PRF to give sufficient Doppler space. However, the longer ranges to typical space targets mean that higher PRFs lead to range ambiguity. Interpulse (pulse-to-pulse) coding can alleviate this trade-off, but the required PRF is outside the normal operating range for the OTHR considered here.

## **6.2 Conclusions of Research**

The OTHR systems as modeled in this thesis have potential for providing limited space surveillance capability, i.e., many typical low earth orbit targets are detectable, but within a very limited coverage region. The ionosphere obscures space targets below a certain elevation angle limit. During normal daytime ionospheric conditions, this limit is above the main lobe of the antenna array, restricting coverage to a sidelobe.

The low sidelobe power levels mean that relative main beam clutter power levels are very high. Also, OTHR design fundamentals limit the achievable pulse repetition frequency such that long integration periods are not possible for fast-moving space targets. For higher pulse repetition frequencies, pulse integration allows detection of targets with radar cross-sections of  $1 \text{ m}^2$  or less, within the coverage region.

Another limitation is that the system has no capability to determine elevation. While a high relative velocity implies that the target is space-based, accurate elevation information cannot be provided, limiting the system's use for orbit determination. Range, range rate (Doppler) and azimuth information will be useful, but several sightings are needed to conclude that a target is space-based.

The space target detection capabilities do not provide sufficiently accurate information to guide other operational activities and do not provide a useful early warning facility of missile or other threats.

Further, the constraints that a space surveillance role places on the system's regular surveillance operations likely preclude one or the other activity from taking place. Given the lack of useful information provided by the system in a space surveillance role,

the normal over-the-horizon surveillance tasks would be the better use of the asset. This conclusion is not surprising given that this is the primary role for which the system was designed.

### **6.3 Significance of Research**

This research provides qualitative justification for not pursuing the use of OTHR networks for space surveillance; rather research into alternative space surveillance methods should be considered.

### **6.4 Recommendations for Action**

Australia's interest in a space surveillance capability remains, but this research shows that an OTHR system is not well-suited for the task. To develop the capability, the Australian Defence Force should continue its investigations into other methods of space surveillance.

A very high frequency (VHF) or ultra high frequency (UHF) space surveillance radar system could overcome many of the disadvantages of OTHR:

- Ionospheric refraction will not be sufficient to return signals to the ground.

This has two effects—firstly, the main beam clutter power is greatly reduced, meaning smaller, more distant targets can be detected. Secondly, the ionosphere does not obscure targets at lower elevation angles. The coverage region is sufficient to provide a useful capability.

- The smaller VHF and UHF wavelengths allow smaller antenna sizes. Thus, steering in both azimuth and elevation would be possible using antennas of a

practical size. The antennas should be flexible, with smaller array groups to allow target detection over a wide area, and larger groups for more accurate positioning.

- The higher VHF and UHF frequencies allow more flexibility in selecting pulse duration, pulse repetition frequency and chirp patterns; these parameters can be optimized for the area under surveillance.

## **6.5 Recommendations for Future Research**

With some modification, the models used in this thesis could be used as the basis for analyzing dedicated VHF or UHF space surveillance systems. This approach might reveal a realistic configuration for a space surveillance system. Such a system requires the ability to steer antenna patterns in both elevation and azimuth.

The competing requirements for wide area surveillance and accurate positioning are well catered for in the radar detection model presented here, with the directionality of receive antennas provided by software-based processing.

## **6.6 Summary**

While an OTHR system provides some ability to detect space targets, the limited coverage region and poor ability to discriminate target positions mean that its value in a space surveillance role is limited. Its usefulness in its intended role means the system is not likely to be retasked to provide this poorer quality capability.

## Bibliography

1. Balanis, Constantine A. *Antenna Theory – Analysis and Design*. New York, USA: John Wiley & Sons, 1997.
2. Barnes, R.I., Gardiner-Garden, R.S. and Harris, T.J. “Real time ionospheric models for the Australian Defence Force”, *Workshop on the Applications of Radio Science 2000*. 122-135. Melbourne, Australia: National Committee for Radio Science, 2000.
3. Cameron, Alex. “The Jindalee Operational Radar Network: Its Architecture and Surveillance Capability”, *IEEE International Radar Conference 1995*. 692-697. Institute of Electrical and Electronic Engineers, 1995.
4. Cannon, Paul S. “Ionospheric Models and Measurements Required By HF Communication System Designers and Operators”, *IEE Colloquium on Propagation Characteristics and Related System Techniques for Beyond Line-of-Sight Radio*. 1/1-1/4. London, United Kingdom: Institution of Electrical Engineers, 1997.
5. Colegrove, Samuel B. “Project Jindalee: From Bare Bones to Operational OTHR”, *IEEE International Radar Conference 2000*. 825-830. Institute of Electrical and Electronic Engineers, 2000.
6. Collin, Robert E. *Antennas and Radio Propagation*. New York, USA: McGraw Hill, 1985.
7. Dandekar, B.S. (and others). *Physics of the Ionosphere for OTH Operation: Chapter 3, OTH Handbook*. Hanscom AFB MA, USA: Air Force Materiel Command, Phillips Laboratory, 1995.
8. Dandekar, B.S. and Buchau, J. *The AN/FPS-118 OTH Radar: Chapter 5, OTH Handbook*. Hanscom AFB MA, USA: Air Force Materiel Command, Phillips Laboratory, 1996.
9. Georges, T.M. and Harlan, J.A. “New Horizons for Over-the-Horizon Radar?”, *IEEE Antennas and Propagation Magazine*, Vol. 36, No. 4: 14-24. Institute of Electrical and Electronic Engineers, August 1994.
10. Hale, Todd B. Course notes, *EENG 668 Advanced Radar Systems Analysis*. Wright-Patterson AFB OH, USA: Graduate School of Engineering and Management, Air Force Institute of Technology, November 2003.

11. Headrick, J.M. "HF Over-the-Horizon Radar", in Skolnik Merrill I. (editor) *The Radar Handbook* (2nd Edition). New York, USA: McGraw-Hill Book Company, 1990.
12. Klemm, Richard. *Principles of space-time adaptive processing*. London, UK: Institution of Electrical Engineers, 2002.
13. Kolosov, Andrei A. and others, translated by Barton, William F. *Osnovy zagorizontnoi radiolokatsii, Over-the-Horizon Radar*. Norwood, MA, USA: Artech House, 1987.
14. Kraus, John D. and Marhefka, Ronald J. *Antennas for all Applications* (3rd Edition). New York, USA: McGraw-Hill Book Company, 2002.
15. Lees, M.L. and Thomas, R.M. "Ionospheric Probing with an HF Radar", *Fourth International Conference on HF Radio Systems and Techniques*. 271-275. London, United Kingdom: Institute of Electrical Engineers, 1998.
16. Naka, F.R. (and others) "Space Surveillance", *Report on Space Surveillance, Asteroids and Comets, and Space Debris*. Vol I. Washington, USA: United States Air Force Scientific Advisory Board, 1997.
17. National Oceanographic and Atmospheric Administration, Environmental Technology Laboratory. "Nominal OTH-B Radar Properties". Excerpt from *Observing Systems*. n. pag. <http://www.etl.noaa.gov/technology/othr/othb.html>. 10 October 2003.
18. Papazoglou, Michael and Krolik, Jeffrey L. "Matched-Field Estimation of Aircraft Altitude from Multiple Over-the-Horizon Radar Revisits", *IEEE Transactions on Signal Processing*, Vol. 47, No. 4. Institute of Electrical and Electronic Engineers, April 1999.
19. Sales, Gary S. *OTH-B Radar System: System Summary*. Hanscom AFB MA, USA: Air Force Systems Command, Phillips Laboratory, 1992.
20. Skolnik, Merrill I. *The Radar Handbook* (2nd Edition). New York, USA: McGraw-Hill Book Company, 1990.
21. Skolnik, Merrill I. *Introduction to Radar Systems* (3rd Edition). New York, USA: McGraw-Hill Book Company, 2001.

22. Tascione, Thomas F. *Introduction to the Space Environment*, 2nd edition. Malabar, USA: Kreiger Publishing, 1994. 114-115
23. Torrel, William C. and Yssel, William J. (editors). *Data Fusion Project Arrangement: Final Report*. San Diego, USA: Space and Naval Systems Center, 1998.
24. Torrel, William C. and Yssel, William J. *Over-the-Horizon Radar Surveillance Sensor Fusion for Enhanced Coordinate Registration*. San Diego, USA: Space and Naval Systems Center, (no date).
25. Ward, J. *Space-Time Adaptive Processing for Airborne Radar*. Lexington, MA, USA: MIT Lincoln Laboratory, 1994.
26. Wheadon, N.S., Whitehouse, J.C., Milsom, J.D. and Herring, R.N. “Ionospheric Modelling and Target Coordinate Registration for HF Skywave Radar”, *HF Radio Systems and Techniques*. 258-266. London, United Kingdom: Institution of Electrical Engineers, 1994.
27. Yssel, William J., Torrel, William C. and Lematta, Robert A. “Measures of Effectiveness for Multiple ROTHR Track Data Fusion (MRTDF)”, *Proceedings, 9th Annual Symposium on Sensor Fusion*. 106-109. San Diego, USA: Space and Naval Systems Center, 1996.
28. Zoubir, A.M. “Statistical Signal Processing for Application to Over-the-Horizon Radar”, *International Conference on Acoustics, Speech and Signal Processing*. VI/113-VI/116. Institute of Electrical and Electronic Engineers, 1994.

## **Vita**

Flight Lieutenant Matthew Colbert was born in Geelong, Victoria, Australia. He joined the Royal Australian Air Force in 1992 through the Australian Defence Force Academy, graduating in 1995 with a Bachelor degree in Electrical Engineering. From 1996 to 2002 he worked in several positions related to communications at both the tactical and operational levels, including at the Air Transportable Telecommunications Unit and at Headquarters Air Command. In 2002, he entered the Graduate School of Engineering at the US Air Force Institute of Technology.

<b>REPORT DOCUMENTATION PAGE</b>					<i>Form Approved OMB No. 074-0188</i>
<p>The public reporting burden for this collection of information is estimated to average 1 hour per response, including the time for reviewing instructions, searching existing data sources, gathering and maintaining the data needed, and completing and reviewing the collection of information. Send comments regarding this burden estimate or any other aspect of the collection of information, including suggestions for reducing this burden to Department of Defense, Washington Headquarters Services, Directorate for Information Operations and Reports (0704-0188), 1215 Jefferson Davis Highway, Suite 1204, Arlington, VA 22202-4302. Respondents should be aware that notwithstanding any other provision of law, no person shall be subject to an penalty for failing to comply with a collection of information if it does not display a currently valid OMB control number.</p> <p><b>PLEASE DO NOT RETURN YOUR FORM TO THE ABOVE ADDRESS.</b></p>					
1. REPORT DATE (DD-MM-YYYY) 23-03-2004		2. REPORT TYPE Master's Thesis		3. DATES COVERED (From – To) March 2003 – March 2004	
4. TITLE AND SUBTITLE  AN ANALYSIS OF THE POTENTIAL FOR USING OVER-THE-HORIZON RADAR SYSTEMS FOR SPACE SURVEILLANCE			5a. CONTRACT NUMBER		
			5b. GRANT NUMBER		
			5c. PROGRAM ELEMENT NUMBER		
6. AUTHOR(S)  Colbert, Matthew J., Flight Lieutenant, Royal Australian Air Force			5d. PROJECT NUMBER		
			5e. TASK NUMBER		
			5f. WORK UNIT NUMBER		
7. PERFORMING ORGANIZATION NAMES(S) AND ADDRESS(S)  Air Force Institute of Technology Graduate School of Engineering and Management (AFIT/EN) 2950 Hobson Way, Building 640 WPAFB OH 45433-8865				8. PERFORMING ORGANIZATION REPORT NUMBER  AFIT/GSS/ENG/04-01	
9. SPONSORING/MONITORING AGENCY NAME(S) AND ADDRESS(ES)  AFHQ R1-6-C105 Russell Offices, Canberra, ACT 2600 Australia				10. SPONSOR/MONITOR'S ACRONYM(S) DD-FSC 11. SPONSOR/MONITOR'S REPORT NUMBER(S) -	
12. DISTRIBUTION/AVAILABILITY STATEMENT  APPROVED FOR PUBLIC RELEASE; DISTRIBUTION UNLIMITED.					
13. SUPPLEMENTARY NOTES					
<p><b>14. ABSTRACT</b>  The Australian Defence Force is investigating the development of a space surveillance system. While several dedicated facilities for surveillance of space are in operation around the world, Australia's Over-The-Horizon Radar (OTHR) network has some potential for this role.  The OTHR operates in the HF band and is constrained by the propagation effects of the ionosphere. A spherically stratified ionospheric model and a model for a nominal OTHR antenna are developed that allow calculation of path propagation, power distribution, and clutter returns. A software-based radar receiver processing system is modeled to determine detection probabilities and the minimum detectable radar cross-section of targets in typical low earth orbit (LEO) trajectories. The high clutter power levels, coupled with long target ranges and high velocities, mean that range-Doppler tradeoffs have a great impact on the resulting detection capabilities.  While the system as modeled has the potential to provide some coverage for LEO targets, operational constraints on the system mean the necessary conditions for detection of space targets would rarely be met while the system is involved in traditional OTHR tasking. Further, the long wavelengths and large antenna beams mean the accuracy of any positioning information is low.</p>					
<p><b>15. SUBJECT TERMS</b> Space Surveillance; Over-the-Horizon Radar</p>					
16. SECURITY CLASSIFICATION OF:		17. LIMITATION OF ABSTRACT	18. NUMBER OF PAGES	19a. NAME OF RESPONSIBLE PERSON Hale, Todd B., Maj, USAF 19b. TELEPHONE NUMBER (Include area code) (937) 785-3636, ext 4639 (todd.hale@afit.edu)	
a. REPORT U	b. ABSTRACT U	c. THIS PAGE U	UU	92	

